Physics – Uspekhi **64** (11) 1125 – 1148 (2021)

REVIEWS OF TOPICAL PROBLEMS PACS numbers: 52.25.Kn, 52.27.Gr, **64.10.+h**, 64.60.F–, 64.70.F–, **71.30.+h**, **72.15.–v**

IN MEMORY OF VLADIMIR EVGEN'EVICH FORTOV

Supercritical fluid of metal vapor plasmas, rare gases, and excitons

A L Khomkin, A S Shumikhin

DOI: https://doi.org/10.3367/UFNe.2020.08.038825

Contents

1. Introduction **1125**

2. Electron jellium: cold ionization **1128**
2.1 Model of an isolated atom in the vicinity of the critical point; 2.2 Calculation of the cold ionization degree in the cell approximation using Hartree–Fock–Slater wave functions; 2.3 Conductivity of electron jellium

3. Collective binding energy: cohesion **1131**
3.1 Bardeen's theory. Cohesion for hydrogen; 3.2 Kratzer potential: pseudopotential for alkali metal atoms; 3.3 Cohesion for alkali metal atoms; 3.4 Cohesion for atoms with a many-electron valence shell

4. 1+ atomic fluid model **1132**
4.1 Thermodynamics of atomic metal vapors in the vicinity of the critical point; 4.2 Critical parameters of metals and their relation to solid-state characteristics; 4.3 Critical density; 4.4 Critical temperature; 4.5 Critical pressure; 4.6 Binodal of the vapor–liquid transition; 4.7 Atomic hydrogen; 4.8 Excitons

5. Atomic–molecular fluid, 2+ model **1137**
5.1 Chemical 2+ model of atomic–molecular hydrogen (deuterium); 5.2 Isotherms and the binodal of the dissociative phase transition

6. Atomic fluid with ionization, 3+ model **1138**
6.1 Helmholtz free energy in the 3+ model; 6.2 Ionization balance equation; 6.3 Equation of state; 6.4 Conductivity

7. Thermal and electrophysical properties of the dense plasma of metal vapors. Comparison with experimental and numerical simulation results **1140**
7.1 Conductivity of metal vapors on supercritical isotherms; 7.2 Caloric and thermal equations of state of metal vapors; 7.3 Conductivity (resistance) of supercritical vapors of metals on isochores

8. Details of calculations of the conductivity of supercritical inert-gas plasmas **1142**
8.1 Ionization balance equation for a dense plasma of inert gases; 8.2 Decrease in the ionization potential; 8.3 Conductivity. Discussion of results

9. Gaseous metal and features of vapor–liquid and insulator–metal transitions in metal vapors **1144**
9.1 Range of existence of a gaseous metal; 9.2 Conductivity in the near-critical domain; 9.3 Minimum of the metal vapor conductivity on isotherms; 9.4 Asymptotic behavior of conductivity isotherms with increasing density

10. Conclusions **1146**

References **1146**

Abstract. We discuss vapor–liquid and dielectric–metal transitions and the metalization process via an exponential increase in conductivity under compression in metal vapors. We investigate the 'cold ionization' mechanism based on a proposed hypothesis on electron jellium existing as a seed of the conduction band in the gas phase. A number of physical models are proposed that combine methods to describe the interaction of atoms as cohesive and collective, caused by the presence of the electron jellium. The parameters of critical points and binodals are calculated for most metals in the Mendeleev periodic table, as well as for hydrogen and excitons. Useful relations between solid-state characteristics of metals and the parameters of critical points are established. Theoretical calculations are compared with experimental results for the equation of state of metal vapors and the conductivity at the critical points, on the binodal, and on near-critical isotherms, with the cold and thermal ionization processes taken into account. We propose the model of a 'jump-like' metalization of inert gases under compression, similar in nature to the Mott transition. We conclude that, in the vicinity of the critical point, metal vapors exhibit properties of metals due to the presence of the cold ionization process.

Keywords: supercritical fluid, vapor–liquid (dielectric–metal) phase transition, cohesion, electron jellium, metalization

A L Khomkin, A S Shumikhin (*)
Joint Institute for High Temperatures, Russian Academy of Sciences, ul. Izhorskaya 13, str. 2, 125412 Moscow, Russian Federation
E-mail: (*) shum_ac@mail.ru

Received 28 May 2020, revised 5 July 2020
Uspekhi Fizicheskikh Nauk **191** (11) 1187 – 1211 (2021)
Translated by S Alekseev

1. Introduction.

In the mid-20th century, Zel'dovich and Landau [1] formulated the problem of the possible coexistence of two phase transitions in metal vapors: vapor–liquid and insulator–metal

transitions. What would their topology on the phase diagram be? Do they occur separately, or is it a single transition? The insulator–Mott-metal transition in solids occurs without a phase transformation of matter and is associated with the deformation of the band structure in cold matter. Does the insulator–metal transition in metal vapors have a similar nature? The questions considered in this review directly relate to this range of issues.

In Fig. 1, we show a phase diagram of matter with the characteristic regions and points indicated. A distinctive feature of the vapor–liquid phase transition is the presence of a critical point at which the derivative of pressure with respect to density vanishes. The density, temperature, and pressure values at this point are called critical parameters. The system of equations for the equality of pressures and chemical potentials leads to a binodal and allows determining the densities of the coexisting liquid and saturated vapor. On the temperature–inverse density phase diagram (see Fig. 1), the solid (SS), liquid (L), and gaseous (Gas) states of matter are marked. The conventional binodal is depicted as a dome. The normal ρ_0 and critical ρ_c densities and the critical temperature T_c are marked. The state of matter with temperature, density, and pressure above the critical ones is usually called a supercritical fluid (SCF) in the literature [2]. This fluid is not a liquid, but rather a kind of gas ($T > T_c$), but with the density of a liquid. A fluid has no boundaries that separate the phases, which distinguishes it from a liquid. Questions about the boundaries of the SCF, the equation of state, etc. are being actively discussed and are not yet fully resolved. A very interesting question is what the SCF is more likely to be: a nonideal gas or an expanded liquid, or even an expanded solid. Resolving this issue determines the choice of theoretical approaches to studying SCF properties. Numerical modeling shows that, on the side of the melting curve at least, many properties of condensed matter are inherent to an SCF, including the preservation of short-range order.

Neutral atomic and molecular substances are mainly being discussed [2, 3]. Supercritical states of metal vapors are distinguished by a rather high critical temperature and hence thermal ionization processes. In [4], the term 'plasma fluid' was proposed for such states. The main feature of the vapor–liquid transition in metal vapors is a significant difference between the properties of the liquid and gaseous phases. The gaseous phase is an almost neutral gas of atoms, and the liquid phase is a highly conductive liquid, a liquid metal. At first glance, the vapor–liquid transition is accompanied by an insulator–metal transition. Here lies an essential difference between such a transition and the traditional vapor–liquid transition, for example, in inert gases. This region of the states of matter is traditionally 'hard' for both theory and experiment. Because of relatively high densities $\rho > \rho_c$, it is difficult to use the well-developed virial approaches (VCM in Fig. 1). At the same time, the condition $\rho < \rho_0$ and the absence of long-range order that it entails do not allow using well-developed approaches of solid state physics.

As an example, we consider the process of isothermal compression of an ideal mixture of atoms, electrons, and ions moving in the direction shown by the arrow in Fig. 1. At low densities in the considered temperature range, the gas is completely ionized. As the density increases, in accordance with the Saha ionization formula, the number of atoms increases, and the ionization degree decreases. In an ideal gas, the ionization degree would decrease to zero under

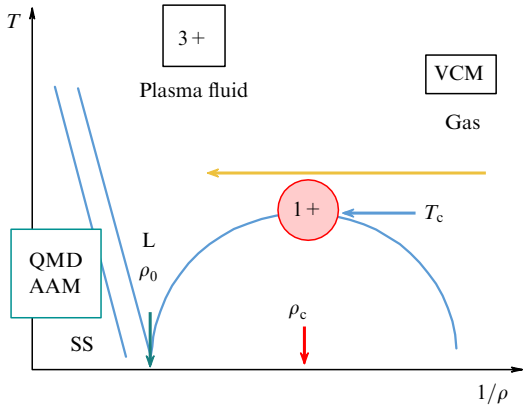

Figure 1. Phase diagram of matter in $T-1/\rho$ coordinates. Normal ρ_0 and critical ρ_c densities and critical temperature T_c are indicated. States of matter: SS, solid; L, liquid; and gas. Method used in calculations: QMD, quantum molecular dynamics; AAM, average atom model; VCM, virial chemical models.

further compression, and the gas would become completely atomic and neutral. In this process, the conductivity also decreases, starting from the conductivity of a rarefied fully ionized gas (determined by the Spitzer formula) to that of a weakly ionized plasma (determined by the Lorentz formula), which also decreases as the density increases. Experiments [5] do indeed demonstrate a decrease in conductivity with an increase in density at moderate densities. But, as the density increases further, the conductivity stops decreasing and its exponential increase almost to metallic values is observed. We call this increase the metalization process, because it occurs smoothly and without jumps. In what follows, we give special attention to metalization processes in vapors during compression.

The coexistence, the features, and the peculiarities of vapor–liquid and insulator–metal transitions manifest themselves in various substances, such as vapors of alkali, transition, and other metals. Some features of the vapor–liquid transition can be observed during the formation of exciton droplets in semiconductors [6] and in atomic hydrogen [7]. An unusual metalization effect (a jump-like increase in conductivity) is also observed under the compression of purely insulating substances, liquid inert gases [8, 9]. Metalization processes can also occur in the atomic component of partially dissociated molecular hydrogen under compression. This leads to a jump in the dissociation degree. A dissociative phase transition (DPT) then occurs [10, 11].

The features and regularities of the processes occurring in the vicinity of the critical points for all the substances mentioned above are also discussed in this review.

Studies of the vapor–liquid transition and metal–vapor metalization processes began a long time ago. The vapors of alkali metals [12–15] and mercury [16, 17], which have a relatively low critical temperature ($\sim$ 2000 K), were the first to be studied experimentally. Comprehensive information on the thermodynamic and transport properties of cesium and rubidium in solid, liquid, and gaseous states is presented in the fundamental collective study [18]. Detailed data on the binodal and conductivity along it for Cs and Rb are also available, e.g., in Hensel's review [19].

Data on the conductivity of alkali metal vapors on the binodal and in the vicinity of the critical point immediately

attracted the attention of theorists, because these data revealed an unusual and rather salient effect: an exponential increase in conductivity by several orders of magnitude on near-critical isotherms under vapor compression. In most studies, this increase was related to an effect well known in plasma physics, a decrease in the ionization potential of an atom, which does lead to an exponential increase in the concentration of thermally ionized electrons and hence to an increase in conductivity. For example, the contribution of electron–atom and ion–atom interactions was discussed in one of the first studies [20]. Corrections to the decrease in the ionization potential depended linearly on the density of atoms, which led to an exponential increase in the density of free (thermally ionized) electrons in weakly ionized vapors, but that was not sufficient. This model did not allow finding critical points, the binodal, or conductivity; in addition, the electron concentrations were also low and strongly dependent on the fitting parameters related to the uncertainty in the electron–atom and ion–atom interaction potentials.

The subsequent development of the theory followed the path of searching for effects that lead to a stronger decrease in the ionization potential. We note a series of studies on cluster–droplet models [21–24]. It was assumed that the conversion of ions into cluster [21, 22] or droplet [24] ions would result in a stronger increase in the concentration of free electrons. At that time, from the 1970s through the 1990s, the parameters of small clusters (comprising fewer than 10 particles) were not known reliably, whereas just these parameters were believed by the authors to be the main source of uncertainty in calculations of the composition. There was an increase in the concentration of charges, but it was insufficient. In addition, the cluster–droplet model did not allow calculating critical points, the binodal, or conductivity.

Numerical calculations of the parameters of small-size clusters (neutral or positively or negatively charged) of alkali and other metals [25] that appeared in the literature allowed a piece by piece count [26]. These calculations showed that the conversion of both positive and negative ions actually occurs. The neutral component of alkali metal vapors near the binodal turned out to be predominantly atomic with a small admixture of molecules; this was also confirmed by independent calculations [27]. The concentration of the charged component was low, and it turned out to be ionic in composition [26], which naturally led to very low conductivity values in the cluster model.

Significant progress in understanding the processes of metalization in alkali metal vapors occurred after the appearance of a series of studies by Likal'ter (see reviews [28, 29]). Although he was the author of the cluster model of ion conversion, he abandoned attempts to find the 'pivotal' decrease in the ionization potential and hypothesized that a major role in conductivity could be played not by thermally ionized free electrons but by bound electrons, whose classically accessible trajectories start overlapping. The overlapping of trajectories leads to the formation of 'percolation' clusters, along which the current flows. This is suggestive of the appearance of a seed of the conduction band. Likal'ter's ideas turned out to be very constructive and allowed calculating not only the conductivity but also the critical points of alkali and many other metals [29]. An equation of state was proposed for 'quasiatoms' — atoms with overlapping classical orbits [30]. Likal'ter's model was largely empirical, because some of its provisions were not derived but only hypothesized.

The approach that we develop is largely stimulated by the ideas expressed in the studies and in personal communications with Likal'ter, now deceased.

Currently, a number of empirical relations are known and used to relate the critical point parameters to various characteristics of matter in the solid, liquid, and gaseous states. These relations are especially relevant for substances for which experimental data on the critical parameters are absent, which is exactly the case with metal vapors. Among these relations, we note the Kopp–Lang rule [31] that relates the critical temperature to the evaporation energy. There are a number of similarity laws, which hold well for inert and molecular gases, that relate the characteristic lines (for example, the Zeno line, the line of unit compressibility) of gases and liquids to the critical parameters [32–34].

As regards metal vapors, we note one of the first studies [35] where the critical point parameters of almost all metals were calculated based on the principle of corresponding states and the method of rectilinear diameter. Alder and Young [36] were the first to have some success in using the equation of state to estimate the critical parameters of metal vapors. A van der Waals equation of state was proposed with the Carnahan–Starling formula used to take the excluded volume into account. The attractive term was chosen proportional to the evaporation energy of metals under normal conditions, which distinguished this equation of state from all those used previously. The introduction of a solid-state characteristic, the vaporization heat, into the equation of state allowed the authors of [36] to calculate the critical parameters for vapors of alkali and many other metals using only two constants, the size of the atom and the vaporization heat, which led to very useful scaling relations. The binodals (the densities of coexisting liquid and gas phases) were not calculated.

The relation between the critical parameters of metal vapors and the ionization potential of atoms was established in [37]. The critical parameters can also be estimated using wide-range equations of state that involve dozens of fitting constants to describe the available experimental results for the solid and liquid states (see, e.g., [38, 39]).

To take interatomic attraction into account, it was proposed in [10] to use the collective energy of interatomic cohesion [40–48], which is a quantity characteristic of the condensed state.

The experimental study of metalization processes in vapors of virtually all other metals was complicated by the high expected values of critical temperatures (see, e.g., [35, 36]). This made the methods of static studies inapplicable. The thermodynamic and transport properties of metals in the vicinity of the critical point are studied by methods of pulsed heating: electric explosions of wires and foils [49–57] and shock-wave techniques [58, 59]. To date, a large amount of experimental data has been obtained on the binodal in the region of the melting curve and on near-critical isotherms and isochores for many metals: Al, Cu, Ni, Fe, and W. For a number of metals, only the conductivity and density were measured in [49–52], and only the internal energy, pressure, density, and resistivity in [53–57]. An exponential increase in the conductivity with increasing density was found on experimental supercritical isotherms [5, 49–52]. Unfortunately, the pulsed measurement technique does not allow direct measurements of the temperature and several other thermodynamic parameters, which complicates the theoretical description of experiments. Nevertheless, a large array of

experimental data on the conductivity of vapors of various metals was processed, systematized in [5], and presented in the form of a set of isotherms for various metals, which is very convenient for theoretical studies. The temperature was reconstructed in [5] using the SESAME equation of state.

The equation of state, the conductivity, and the thermal conductivity of metals, mostly in the solid state but also in the expanded state, are currently being investigated by numerical methods using the quantum molecular dynamics (QMD) method [60–69], the path integral Monte Carlo (PIMC) method [70, 71], and the average-atom method (AAM) (see, e.g., [72, 73]). Arguably, *ab initio* calculations, which can actually be called numerical simulations, have become a new, even if somewhat special, field in modern theoretical physics. Without a doubt, numerical simulation methods have numerous advantages: they allow obtaining data in the phase diagram regions that are still inaccessible to theory and experiment. We actively use these data in our work. Unfortunately, these approaches also have certain drawbacks. For example, in QMD codes, the wave functions of all electron states, including inner-shell electrons, the valence electrons that form the conduction band, and thermally ionized electrons, are sought in the form of an expansion in plane waves, and their contributions are then quite difficult to separate. Problems also arise at high rarefaction levels. As a result, it is usually rather difficult to interpret the results of numerical QMD calculations in detail, which complicates the formulation of physical models of the relevant processes.

High temperatures on near-critical isotherms in metal vapors have led to a number of theoretical studies where the observed exponential increase in conductivity, as in the case of alkali metal vapors, was again related to an increase in the concentration of thermally ionized electrons due to the effect of a decrease in the ionization potential [74–79]. This time, however, the role of the main term responsible for the decrease in the ionization potential was assigned to the contribution of the Coulomb interaction between free charges. A very deep extrapolation of the Debye energy of the interaction of free charges or its modification for the decrease in the ionization potential allowed explaining the experiments in [49–52], but at the price of assuming a plasma phase transition [80, 81] in approaching the normal density and turning a blind eye to the fact that the use of the same model in thermodynamics resulted in the loss of stability in the equation of state, which was not confirmed by either subsequent experiments [53] or numerical simulations [53, 60, 61, 67].

The range of problems discussed in this review includes the question of the vapor–liquid phase transition in atomic hydrogen and vapors of excitons, which resemble hydrogen gas in many respects. The model of a plasma phase transition was very actively advanced in this field [80–83]. Using our results on phase transitions in metal vapors, we show that another interpretation of this effect is also possible. Because atomic hydrogen and exciton vapor are not metal vapors in the generally accepted sense, we briefly review the literature in Sections 4.7 and 4.8.

Metalization effects have also been observed under compression in inert gases, which are fundamentally insulator gases [84–87]. A high, nearly metallic, level of conductivity of the plasma of inert gas vapors was observed at relatively low temperatures ($T \approx 5{,}000-15{,}000$ K) but at high densities and pressures. We emphasize that the data were obtained under shock-wave compression of liquid inert gases. They demonstrate a sharp, almost abrupt increase in conductivity [84–87], in contrast to the previously obtained high-temperature data (albeit essentially density-independent and recorded under the compression of gaseous inert gases) [88, 89]. The observed effect largely resembles the metalization of metal vapors, differing from it by a nearly jump-like increase in conductivity. An increase in conductivity is also revealed in the data of numerous QMD calculations for helium and other inert gases [90–93].

Physical models of the metalization effect in inert gases were proposed in [8, 94–97]. The increase in conductivity under compression was explained traditionally by an increase in the concentration of free (thermally ionized) electrons due to a decrease in the ionization potential caused by the interaction of free particles in the continuous spectrum [94–96]. In [8, 97], this interaction was mainly due to interatomic repulsion and the effects of spectrum rearrangement in the 'bounded atom' model with a moderate value of Coulomb nonideality effects. Taking all these factors into account leads to an increase in the concentration of thermally ionized electrons, but only at higher densities.

Under the shock-wave compression of hydrogen and deuterium that are in the molecular state, features on the Hugoniot shock adiabats were observed in [98–102]. These experiments attracted considerable attention, because some of them [98] demonstrated the anomalous compressibility of deuterium. A large number of various models were proposed to explain the anomalies observed on shock adiabats, but a generally accepted physical picture of the phenomenon is still unavailable [103]. Anomalies were indicative of the possible presence of an unusual new phase transition [104].

In our approach, all the phenomena noted in the Introduction occurring in dense metal vapors, in atomic and molecular hydrogen, and in exciton gas and inert gases, are treated in a uniform manner using the proposed series of SCF models: the 1+ model (atomic gas + jellium); the 2+ model (atomic–molecular gas + jellium), and the 3+ model (atomic plasma + jellium). All the proposed SCF models are related by a common set of assumptions and approximations:

(1) The existence in the gas phase of the electron jellium formed by the tails of wave functions of bound electrons lying outside the Wigner–Seitz (WS) atomic cells. The term 'cold ionization' is used to indicate the formation of electron jellium (a seed of the conduction band).

(2) Cohesive collective interaction of atoms instead of the pairwise additive interaction used in virial approaches. Cohesive attraction and electron jellium are always present simultaneously.

(3) Limited compressibility (excluded volume), described in the Carnahan–Starling approximation.

(4) The total conductivity of dense metal vapors determined by the total conductivity of thermal electrons (the 3+ model) and of jellium electrons (the 1+, 2+, and 3+ models).

2. Electron jellium: cold ionization

As a solid metal expands, the conduction band undergoes transformations. In a certain form, it persists in the liquid phase. We assumed that, under the transition to the SCF state, the traces of the conduction band do not disappear jump-wise but remain in the gas phase as well. We called these electrons electron jellium. In the gas phase, electron jellium is formed due to the overlap of the tails of the bound electron wave functions lying outside the WS atomic cell. Jellium

electrons can move from cell to cell and thus contribute to the conductivity of metal vapors.

That conducting electron jellium can possibly exist in the gas phase is indicated by the experimentally observed rather high conductivity of vapors of alkali metals (Cs and Rb) at critical points and in the near-critical region at low temperatures ($T \sim 2{,}000$ K) [12, 14, 15].

Attempts to explain the conductivity of alkali metal vapors in the vicinity of the critical point by motion along the liquid branch of the binodal (see, e.g., [105, 106]) or along the gas branch of the binodal (see the Introduction) have not been successful.

2.1 Model of an isolated atom in the vicinity of the critical point

Another important aspect underlying our concept and methodology for calculating the electron jellium concentration in the gaseous state of metal vapors is the need to improve the concept of an 'isolated atom.' An atom is a particle made up of a nucleus and bound electrons; it has an extended internal structure. To calculate the spectrum and wave functions of bound states of an atom, the Schrödinger equation is solved with the standard boundary condition, that of the vanishing of the wave functions at infinity. This is exactly the model of an isolated atom. The spectrum of bound states thus found is used, for example, to calculate the partition function of an atom, but the obtained wave functions of bound electrons of an atom are not used explicitly in calculations of the equation of state, composition, or numerous transfer coefficients. However, they are different from zero in the entire space, to infinity. In approaching the critical region, the approximation of an isolated atom must be corrected, because, in a gas with the atom density n_a, the space occupied by one atom is always bounded and is determined by the volume of the WS cell with radius R_a:

$$R_a = \left(\frac{3}{4\pi n_a}\right)^{1/3}. \tag{1}$$

The wave function of a bound electron decays exponentially at infinity, and therefore the effect of the bounded volume occupied by one atom in a rarefied gas is insignificant. We have noted that the fraction of the density of bound electrons lying outside the WS cell can be quite significant in the vicinity of the critical points of metal vapors. These are the electrons that form the electron jellium in our model. The ratio of the density of jellium electrons n_j to the density of atoms n_a can be called the cold ionization degree, $\alpha_j = n_j/n_a$.

2.2 Calculation of the cold ionization degree in the cell approximation using Hartree–Fock–Slater wave functions

As the first approximation in solving the very complex problem of the electron density distribution in an atomic gas, we consider an iterative procedure that is fairly reasonable in our opinion.

We assume that the wave function $\Psi^i(r)$ of the bound ith electron is known in the isolated atom approximation. The contribution to the electron jellium is made by the tails of the density of bound electrons of all atoms, both the given one and all those surrounding it.

Knowing the wave function of the ith electron of an isolated atom, we can in the first approximation calculate the fraction of the electron density involved in the formation of electron jellium in the cell approximation. The quantity α_j^i is determined by integrating $|\Psi^i(r)|^2$ over the region outside the WS cell (this corresponds to the contribution of the surrounding cells to the chosen one) and by the contribution of the constant background inside the cell $|\Psi^i(y_a)|^2$ (which corresponds to the contribution to the jellium from this cell):

$$\alpha_j^i = \int_{y_a}^{\infty} |\Psi^i(r)|^2 r^2 \, dr + \frac{y_a^3}{3} |\Psi^i(y_a)|^2, \tag{2}$$

where $y_a = R_a/a_0$ is the WS cell radius expressed in atomic units. The total electron density is conserved and the WS cell remains electrically neutral.

Data on the wave functions of an isolated atom calculated numerically by the Hartree–Fock method are presented in [107], for all elements with the atomic number up to 54.

The wave function $\Psi^i(\mathbf{r})$ of an arbitrary ith-atom electron that is in a certain quantum state can be represented as an expansion in the Slater orbitals $\chi_{\lambda,p}(r,\theta,\phi)$:

$$\Psi^i(\mathbf{r}) = \sum_{\lambda,p} C_{\lambda,p}\, \chi_{\lambda,p}(r,\theta,\phi). \tag{3}$$

The constants of Slater orbitals (3) are presented in [107] in the form of tables for all electron states.

We can formally calculate α_j^i for all electrons of an arbitrary atom. Their sum then gives an approximation of the sought cold ionization degree. In our calculations, we used the data in [107] only for valence electrons, because the contribution of the ionic core electrons is small under the assumed conditions and does not affect the total $\alpha_j = \sum_i \alpha_j^i$. Moreover, it must be borne in mind that, in the vicinity of the critical point, even valence electrons participate in the formation of electron jellium only partly. In approaching the normal density of the metal, all valence electrons gradually become involved in the formation of the electron jellium, and α_j tends to the total valence.

As an example, in Fig. 2, we present the results of our calculations of the cold ionization degree α_j for various metals as a function of y_a in accordance with relation (2). It is small at low densities (large y_a). As the density increases, α_j tends to the valence of the element. At the critical point for Al, for example, $y_a \sim 5$, whereas for the normal-state metal, $y_a \sim 3$. The critical density of Cs corresponds to $y_a \sim 9.8$.

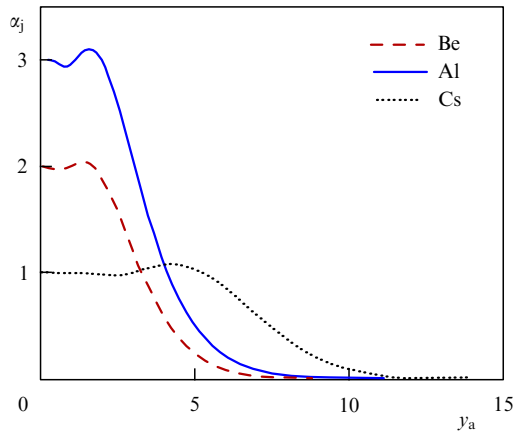

Figure 2. Cold ionization degree for Al, Be, and Cs as a function of the WS cell radius expressed in atomic units.

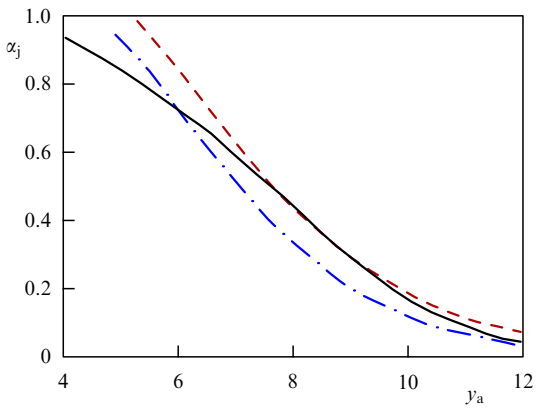

Figure 3. Cold ionization degree α_j as a function of the dimensionless WS cell radius for rubidium: solid line, calculation in accordance with Eqn (4); dashed-dotted line, Hartree–Fock calculation (2); dashed line, calculation in accordance with (5).

Analyzing the calculated dependence of the cold ionization degree α_j on the density y_a allows us to conclude that the electron state in dense metal vapors is no longer a purely bound state, as was thought previously, but rather is mixed, as had been noted by Likal'ter [28]: an electron in the negative-energy ground state is simultaneously in a localized bound state and in a delocalized state of the jellium.

In [108], we compared the results of calculating α_j in accordance with (2) with the data obtained by other methods. For example, for atoms with one valence s-electron, the Schrödinger equation can be solved with the Wigner boundary condition, which amounts to the vanishing of the derivative of the wave function at the boundary of the WS cell. The wave function $\Psi_W(\mathbf{r})$ found this way for the ground state of a system of atoms does not vanish at the boundary of the WS cell, and we can then estimate the cold ionization degree from the relation

$$\alpha_j^W = \left[\frac{4\pi R_a^3}{3}\left|\Psi_W(R_a)\right|^2\right]. \tag{4}$$

We note that, for any boundary condition except the hard-wall one, the wave function is nonzero at the boundary of the WS cell, thus making the existence of electron jellium possible.

In the embedded atom model (EAM) [109–111], which is widely used to calculate the properties of liquid and weakly expanded metals, electron jellium (the transformed solid-state conduction band) becomes a fundamental concept. In [48], a relation is given, obtained from *ab initio* calculations, that allows estimating the ratio of the electron jellium density to the metal density n_m under normal conditions depending on the current density of the metal:

$$\alpha_j^{EAM} = \frac{n_j}{n_m}. \tag{5}$$

In Fig. 3, we show the dependence of the cold ionization degree α_j on the dimensionless radius of the WS cell for rubidium, calculated by various methods [108]. The solid line shows the result of calculations in accordance with formula (4), the dashed-dotted line, the Hartree–Fock calculation (2), and the dashed line, calculations in accordance with formula (5). Similar calculations for cesium and aluminum are also given in [108].

As can be seen from the figure, calculations by different methods give close and yet different results for the cold ionization degree. This is unsurprising because, as noted, all calculation methods are approximate. Arguably, calculations using formula (5) work well at low rarefaction degrees, near the normal density of the metal. Calculations using the Hartree–Fock method, Eqn (2), on the contrary, work well at high rarefaction, when the conduction band just starts to form and the wave functions of valence electrons are distorted weakly, being close to the wave functions for an isolated atom.

2.3 Conductivity of electron jellium

Jellium electrons can move from cell to cell. It is natural to assume that they mostly move between neighboring cells, in contrast to the conduction electrons in a metal. As a result, conductivity appears in a 'cold' atomic gas without thermal ionization processes. To estimate the conductivity of jellium electrons, we use the Regel–Ioffe formula for the minimum metallic conductivity [112] with the intercellular transport mechanism taken into account:

$$\sigma_j = n_j \frac{e^2}{m_e}\tau, \tag{6}$$

where e and m_e are the electron charge and mass, $n_j = \alpha_j n_a$ is the jellium electron density, and τ is the mean free time. The time τ is defined as the time of flight over the intercellular distance, equal to twice the WS cell radius $2R_a$ ($2y_a$ in atomic units), with the Fermi velocity $v_F = p_F/m_e$:

$$\frac{\tau}{m_e} = \frac{2R_a}{p_F}, \tag{7}$$

where $p_F = (3\pi^2 n_j)^2\,\hbar$ is the Fermi momentum for the jellium electrons. As a result, we obtain the following expression for calculating the conductivity of jellium electrons:

$$\sigma_j = n_j^{2/3}\,\frac{e^2}{9\times 10^{11}}\,\frac{2y_a a_0}{(3\pi^2)^{1/3}\hbar}. \tag{8}$$

The conductivity of jellium electrons is determined by their concentration n_j, related to the density of atoms, and by the explicit dependence on the density of atoms via y_a, the size of the atomic cell expressed in atomic units. There is no temperature dependence. The dimension of all quantities in (8) is CGSE, and the conductivity is then expressed in $\Omega^{-1}\,\mathrm{cm}^{-1}$.

To evaluate the conductivity of vapors, for example, of Cs, Al, and Be, it suffices to specify their density using the plots in Fig. 2, find α_j, and then use (8) to calculate the conductivity:

$$\rho \to n_a \to y_a \to n_j = \alpha_j n_a \to \sigma_j. \tag{9}$$

In Table 1, we present a step-by-step calculation of the conductivity at the critical points of some metals (Be, Al, Rb, and Cs). For cesium and rubidium, the experimental density at the critical point is shown [13], and for aluminum and beryllium, the density at the critical point that we found in [113]. The calculated values of the cold ionization degree α_j are indicated but can also be estimated from the plot in Fig. 2. The experimentally obtained values of conductivity for cesium and rubidium at the critical point

Table 1. Conductivity at the critical point for different metals.

Metal	ρ_{cr}, g cm^{-3}	n_a, cm^{-3}	y_a	α_j	n_j, cm^{-3}	σ, Ω^{-1} cm^{-1}
Cs	0.38	1.71×10^{21}	9.79	0.113	1.93×10^{20}	272
Rb	0.29	2.04×10^{21}	9.23	0.18	3.67×10^{20}	394
Al	0.6	1.33×10^{22}	4.94	0.54	7.18×10^{21}	1970
Be	0.38	2.53×10^{22}	4.0	0.6	1.52×10^{22}	2000

are $250 \pm 150\,\Omega^{-1}$ cm^{-1} [14]. For other metals, the critical-point conductivity values are unknown.

A comparison with the experimental data for the conductivity of alkali metal vapors at the critical point provides some substantiation for the hypothesis on the possible existence of electron jellium as a seed of the conduction band in the gaseous phase. The existence of electron jellium leads to the appearance of a number of new effects: the cold ionization process, a new conductivity channel, and a new type of interatomic interaction for metal vapors: cohesion. In the presence of cold ionization processes, metal vapors can be called a gaseous metal.

3. Collective binding energy: cohesion

The presence of conduction electrons in metals gives rise to a particular type of binding energy, cohesion, occurring due to the bonding of ionic cores with conduction electrons. In [10, 114], it was proposed that the quantum collective binding energy — cohesion — be used to describe the interatomic interaction in the plasma fluid of hydrogen and metal vapors. This alternative to the pairwise additive scheme for taking interatomic interaction into account should be considered a hypothesis.

3.1 Bardeen's theory. Cohesion for hydrogen

Bardeen [40] addressed the problem of the appearance of a collective binding energy (cohesion) in an ordered system of N_a atoms with one valence s-electron located in a volume V. In such a system, collective electron states are possible like the Bloch waves formed by electrons that reside in bound states due to the overlap of their wave functions. The appearance of such electrons gives rise to cohesion. Bardeen found the spectrum of these electron states [40]:

$$E_B(k) = E(0) + a\,\frac{\hbar^2 k^2}{2m}\,, \tag{10}$$

where $\hbar$ is the Planck constant, k is the wave vector of the electron, m is its mass, and $E(0)$ is the energy of the electron ground state corresponding to the zero momentum of collective motion. Relation (10) describes the energy (the electron term) of a system of atoms as a whole. Averaging (10) over the Fermi distribution, in the low-temperature limit we obtain the energy per atom as

$$E_a = E(0) + a\,\frac{3}{5}\,E_F\,, \tag{11}$$

where $E_F = (3\pi^2 n_a^2)^{2/3}\hbar^2/2m$ is the Fermi energy and $n_a = N_a/V$ is the density of atoms. According to Wigner, the binding energy E_{coh} of an atom with the medium is determined by the difference between the energy E_a and the binding energy of an electron in an isolated atom ($-$Ry). For hydrogen,

$$E_{coh} = E_a + \mathrm{Ry}\,, \tag{12}$$

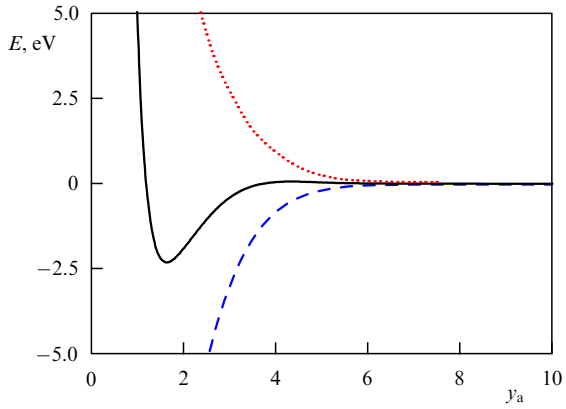

Figure 4. Binding energy — cohesion — for hydrogen as a function of the dimensionless WS cell radius y_a. Dashed line: ground state energy; dotted line: kinetic energy of delocalized electrons; solid line: collective binding energy.

where Ry is the binding energy of an isolated hydrogen atom.

The coefficient a found by Bardeen takes the fraction of delocalized electrons (the first factor) and the inhomogeneity of the wave function (the second factor) into account,

$$a = \left(\frac{4\pi R_a^3}{3}\,\Psi_0^2(R_a)\right)\left(\frac{R}{\Psi_1(R)}\,\frac{\mathrm{d}\Psi_1(R)}{\mathrm{d}R}\right)_{R=R_a}\,, \tag{13}$$

where $\Psi_0(R)$ and $\Psi_1(R)$ are solutions of the Schrödinger equation for the respective s and p states. For hydrogen, the solutions that are finite at the origin are well known and can be expressed in terms of the confluent hypergeometric function $F(a, b, x)$:

$$\Psi_l(R) = A_l \exp(-kR) R^l F\left(l + 1 - \frac{1}{ka_0}\,, 2l + 1, 2kR\right). \tag{14}$$

Here, $k^2 = 2m|E|/\hbar^2$, $a_0 = \hbar^2/me^2$ is the Bohr radius. To calculate E_{coh} in (12), we must find the ground state energy $E(0)$ and calculate a. The ground state energy $E(0)$ can be determined from the solution of the Schrödinger equation with the WS boundary condition on the cell boundary,

$$\left.\frac{\mathrm{d}\Psi_0(R)}{\mathrm{d}R}\right|_{R=R_a} = 0\,, \tag{15}$$

with the normalization constant A_0 to be found from the normalization condition $4\pi\int_0^{R_a}(\Psi_0(R))^2 R^2\,\mathrm{d}R = 1$. The normalization constant A_1 is not needed, because Eqn (13) involves the logarithmic derivative of $E(0)$-dependent $\Psi_1(R)$,

$$\Psi_1(R) = A_1 \exp(-k_0 R) R^l F\left(2 - \frac{1}{ka_0}\,, 2 + 1, 2kR\right), \tag{16}$$

where $k_0^2 = 2m|E(0)|/\hbar^2$.

Formulas (11)–(13) define cohesion, and we show its main components in Fig. 4: the ground state energy (dashed line), the kinetic energy of delocalized electrons (dotted line), and the dependence of the binding energy of hydrogen atoms $E_{\rm coh}$, calculated in [10], on the WS cell radius (expressed in Bohr radii) (solid curve). It can be seen that a noticeable interaction of atoms occurs when they are sufficiently close to each other (at several a_0). The binding energy has a rather deep minimum of ~ 2.5 eV.

3.2 Kratzer potential: pseudopotential for alkali metal atoms

In dealing with the interatomic interaction of alkali metal atoms, the presence of inner-shell electrons must be taken into account. This problem was solved previously in the semiclassical approximation [41, 42]. In [114], the use of the Kratzer potential [44] was proposed to describe the interaction of a valence electron with an atomic core. This potential coincides with the Coulomb one at long distances, but contains a repulsive branch at short distances. The main advantage of the Kratzer potential is its simplicity and the 'hydrogen-like' nature of solutions of the Schrödinger equation with it:

$$V_{\rm Kr}(r) = -2D\left(\frac{a}{r} - \frac{1}{2}\frac{a^2}{r^2}\right). \tag{17}$$

We choose the parameters of potential (17) based on two conditions. At long distances, it must coincide with the Coulomb potential, and its ground electron level E_0 must coincide with the energy of the ground level of an isolated alkali metal atom $-I$:

$$2Da = e^2, \tag{18}$$

$$E_0 = -I. \tag{19}$$

Thus, we assume that all the features of the interaction of a valence electron with an ionic core are determined by the ionization potential. In [114], relations were obtained between the parameters of potential (17) and the ionization potential of the ground state I of an alkali metal atom (expressed in atomic units),

$$\frac{D}{\rm Ry} = \frac{1}{\left(\sqrt{{\rm Ry}/I} - 1/2\right)^2 - 1/4}, \tag{20}$$

$$\frac{a}{a_0} = \left(\sqrt{\frac{\rm Ry}{I}} - \frac{1}{2}\right)^2 - \frac{1}{4}, \tag{21}$$

and Kratzer potentials were calculated for all alkali metals.

3.3 Cohesion for alkali metal atoms

To calculate the cohesive energy of interaction of alkali metal atoms with the density $n_{\rm a} = N_{\rm a}/V$, we again use Bardeen's results (11)–(13) [40]. Repeating calculations similar to those given for hydrogen (see the details in [10]), we can obtain the desired relations for the cohesion of alkali metals [114]. We note that the experimentally measured critical density of cesium vapor corresponds to $R_{\rm a}/a_0 \sim 9.4$, which is close to the vanishing point of the calculated cohesion ($R_{\rm a}/a_0 \sim 10$). This confirms Stishov's hypothesis [115] that the critical density of the transition to the liquid state is close to the point of the second change of sign by cohesion. The coordinate and the value of the cohesive energy at the minimum allow finding the sublimation energy $E_{\rm subl}$ and the lattice parameter L. The radius of the hard core $R_{\rm HS}$ and the critical density $\rho_{\rm cr}$ are determined by the coordinates at which cohesion vanishes. Our calculations in [114] are in good agreement with the experimental data.

3.4 Cohesion for atoms with a many-electron valence shell

The Bardeen formula becomes virtually unusable for atoms with a complex many-electron valence shell. In [47, 48], a simple and universal binding energy relation (UBER) was proposed based on the processing of the results of many numerical calculations of the cohesive binding energy, adhesion, chemisorption, and even the binding energy of atoms in molecules. It turned out that, for a particular choice of scale parameters, all these calculations can be described by a single, reasonably simple, and universal function $E_{\rm UBER}(a^*)$ of the dimensionless rarefaction parameter a^*. For the cohesive energy, these universal relations take the form

$$E_{\rm UBER}(a^*) = \Delta E E^*(a^*), \tag{22}$$

$$E^*(a^*) = -(1 + a^*)\exp(-a^*), \tag{23}$$

$$a^* = \frac{R_{\rm a} - R_0}{l}. \tag{24}$$

In (22), ΔE is the binding energy of a metal atom at the minimum of cohesion, which determines the evaporation energy under normal conditions, and $E^*(a^*)$ is a universal dimensionless scaling function. The dimensionless rarefaction parameter a^* is expressed in terms of the WS cell radii for the normal R_0 and current $R_{\rm a}$ metal densities. In (24), l is the scaling length, which can be defined in terms of the second derivative of the binding energy with respect to distance and may be related to the isothermal elastic modulus B of a solid metal. The result obtained in [48] under normal conditions, when thermal effects can be neglected, is

$$l = \sqrt{\frac{\Delta E}{{\rm d}^2E/{\rm d}a^{*2}}} = \sqrt{\frac{\Delta E}{12\pi B R_0}}. \tag{25}$$

The normal density (cell radius R_0), evaporation energy ΔE, and isothermal elastic modulus B are known for most metals and are tabulated in [48]. Relations (22)–(24) then allow obtaining the cohesive binding energy both in the normal-density region and in the region where the density vanishes. According to [115], it is this latter region that determines the vapor–liquid phase transition point.

4. 1+ atomic fluid model

In the immediate vicinity of the critical point of metal vapors, thermal ionization processes can be neglected in the first approximation. This is suggested by numerous calculations in the framework of virial chemical models [26, 27]. For the near-critical region, we have proposed a one-component model of a metal vapor fluid whose free energy takes the collective binding energy (cohesion) into account, and calculations of the cold ionization degree and conductivity account for electron jellium.

4.1 Thermodynamics of atomic metal vapors in the vicinity of the critical point

We consider an ensemble of $N_{\rm a}$ atoms located in a volume V at a temperature $k_{\rm B}T = 1/\beta$. We then have the Helmholtz free

energy

$$F = F_{\rm IG} + F_{\rm HS} + F_{\rm INT}\,, \tag{26}$$

where

$$F_{\rm IG} = -N_{\rm a}k_{\rm B}T\ln\left(\frac{eVg_{\rm a}\exp(\beta I)}{N_{\rm a}\lambda_{\rm a}^3}\right) \tag{27}$$

is the contribution of ideal gas atoms, and $\lambda_{\rm a} = [2\pi\hbar^2/(m_{\rm a}k_{\rm B}T)]^{1/2}$, $g_{\rm a}$, and I are, respectively, the thermal wavelength of the atom, its statistical weight, and its ionization potential. The second term in (26) describes the effect of the excluded volume. To describe it in our model, we use the Carnahan–Starling approximation, expressed in terms of the packing parameter η,

$$F_{\rm HS} = -N_{\rm a}k_{\rm B}T\,\frac{4\eta - 3\eta^2}{(1-\eta)^2}\,, \quad \eta = \frac{4}{3}\,\pi\,\frac{N_{\rm a}}{V}\,R_{\rm HS}^3\,, \tag{28}$$

where $R_{\rm HS}$ is the effective radius of the solid core of an atom. The first two terms in (26) provide a good description of the thermodynamics of a system of hard spheres in a wide range of parameters. In $F_{\rm INT}$, only the interatomic interaction is taken into account based on the hypothesis on the decisive role of the quantum collective energy of binding between atoms (cohesion):

$$F_{\rm INT} = \frac{1}{2}\,N_{\rm a}E_{\rm coh}(y_{\rm a})\,. \tag{29}$$

In (28), we normally choose $R_{\rm HS}$ to be the radius at which the cohesion changes sign and becomes a rapidly increasing positive quantity [108, 114]. When using UBER relations (22)–(24) for cohesion, $R_{\rm HS}$ is determined analytically from the equation $1 + a^* = 0$. This implies the simple relation $R_{\rm HS} = R_0 - l$. The dimensionless variable $y_{\rm a} = R_{\rm a}/a_0$ defines the current radius of the WS cell in units of the Bohr radius a_0. If we move to atomic units in formula (24) for the scaling radius, then

$$a^* = \frac{y_{\rm a} - y_0}{l_0}\,, \tag{30}$$

where $y_0 = R_0/a_0$ is the dimensionless radius of the normal-density WS cell and l_0 is the scaling length l in (25), expressed in Bohr radii. Finally, for cohesion, we obtain the formula

$$E_{\rm coh}(y_{\rm a}) = E_{\rm UBER}(\Delta E, y_0, l_0, y_{\rm a})\,. \tag{31}$$

As a result, for the Helmholtz free energy of the 1+ model, we obtain

$$F = -N_{\rm a}k_{\rm B}T\ln\left(\frac{eVg_{\rm a}\exp(\beta I)}{N_{\rm a}\lambda_{\rm a}^3}\right) + N_{\rm a}k_{\rm B}T\,\frac{4\eta - 3\eta^2}{(1-\eta)^2} + \frac{1}{2}\,N_{\rm a}E_{\rm coh}(y_{\rm a})\,. \tag{32}$$

Knowing the free energy, we can obtain the pressure $P = -\partial F/\partial V$, the internal energy $E = \partial\beta F/\partial\beta$, and, whenever necessary, any other thermodynamic function

$$P = P_{\rm IG} + P_{\rm HS} + P_{\rm INT}\,, \tag{33}$$

where

$$P_{\rm IG} + P_{\rm HS} = k_{\rm B}T\,\frac{N_{\rm a}}{V}\left(1 + \frac{4-2\eta}{(1-\eta)^3}\,\eta\right), \tag{34}$$

$$P_{\rm INT} = -\frac{1}{2}\,\frac{N_{\rm a}}{V}\,\frac{\partial E_{\rm coh}(y_{\rm a})}{\partial y_{\rm a}}\,\frac{y_{\rm a}}{3}\,. \tag{35}$$

4.2 Critical parameters of metals and their relation to solid-state characteristics

Expression (32) for the free energy allows calculating all thermodynamic functions and finding the critical parameters by determining the coordinates ($\rho_{\rm cr}$, $T_{\rm cr}$, $P_{\rm cr}$) of the inflection points of the isotherm. In Table 2, we show the results of our calculations (boldfaced) for some metals from the Mendeleev periodic table, along with the original data ΔE, y_0, and l_0. Experimental data for alkali metals [13, 19] are italicized. The results of our calculations are presented in more detail in [113, 116–119].

4.3 Critical density

According to Stishov's results [115], the critical density of the vapor–liquid transition in metal vapors is close to the density at which the cohesive energy vanishes. Unfortunately, cohesion in the UBER form, Eqn (22), does not have such a characteristic point, in contrast to the analytic result for vapors of alkali metals [114] and hydrogen [10]. Nevertheless, because the only parameter that determines the 'smallness' of dimensionless cohesion (22) is the dimensionless rarefaction parameter a^*, it can be expected to be the same at the critical point of all metals. This conclusion is confirmed by our calculations in [113], where we show that the value of this parameter is close to three with a sufficiently good accuracy. Using this fact and the relation $a^*_{\rm cr} = (y_{\rm cr} - y_0)/l_0$, we obtain the dimensionless cell radius corresponding to the critical density $y_{\rm cr}$ and the tabulated quantities y_0 and l_0:

$$y_{\rm cr} = y_0 + 3l_0\,. \tag{36}$$

Using (36) for the critical density $\rho_{\rm cr}$, we obtain a relation connecting this density to characteristics of a solid state:

$$\rho_{\rm cr} = 2.68\,\frac{A}{y_{\rm cr}^3} = 2.68\,\frac{A}{(y_0 + 3l_0)^3}\,. \tag{37}$$

Here, A is the atomic weight, and the result obtained is expressed in g cm^{-3}.

4.4 Critical temperature

The Kopp–Lang rule [31], known from the literature, relates the critical temperature $T_{\rm cr}$ and the enthalpy of vaporization of molecular and inert gases, which, under normal conditions, coincides with the evaporation (sublimation) energy ΔE. The rule states that there is a linear relation between them:

$$T_{\rm cr} = \eta\Delta E\,. \tag{38}$$

The values of the coefficient η are slightly different for different substances, but are generally close to 0.15–0.25. Using the obtained array of data for metal vapors, the dependence of the critical temperature on the evaporation energy was plotted in [113]: it turns out that $\eta \approx 0.2$. Remarkably, this value coincides with the dimensionless value of $E^*(a^*_{\rm cr})$. Indeed, as we have established, $a_{\rm cr} \approx 3$ at the critical point, and therefore $E^*(a^*_{\rm cr}) = (1+3)\exp(-3) = 0.199$, which corresponds to $\eta = 0.2$. As a result, a relation is proposed that connects the critical temperature with para-

Table 2. E_{UBER} parameters and critical parameters of metals.

Metal	ΔE, eV	y_0	l_0	ρ_{cr}, g cm^{-3}	T_{cr}, K	P_{cr}, atm	Reference
Alkali metals							
Cs	—	—	—	*0.38*	*1924*	*92.5*	[13]
—	—	—	—	0.54	1942	233	[36]
—	—	—	—	0.43	2057	144	[35]
—	0.827	5.65	1.5	**0.43**	**1950**	**260**	
Rb	—	—	—	*0.29*	*2017*	*124.5*	[13]
—	—	—	—	0.3	2060	123	[29]
—	—	—	—	0.43	2061	308	[36]
—	—	—	—	0.346	2093	159	[35]
—	0.858	5.19	1.24	**0.36**	**2020**	**350**	
Na	—	—	—	*0.3*	*2485*	*248*	[19]
—	—	—	—	0.15	2535	282	[29]
—	—	—	—	0.27	2635	921	[36]
—	—	—	—	0.206	2573	275	[35]
—	1.13	3.92	1.06	**0.18**	**2750**	**900**	
K	—	—	—	*0.17*	*2178*	*150*	[19]
—	—	—	—	0.16	2140	144	[29]
—	—	—	—	0.24	2185	396	[36]
—	0.941	4.86	1.23	**0.18**	**2300**	**450**	
Alkali-earth metals							
Be	—	—	—	0.26	5400	460	[36]
—	—	—	—	0.35	9200	12,200	[29]
—	—	—	—	0.55	8080	11,700	[35]
—	3.33	2.359	0.589	**0.38**	**8050**	**14,000**	
Mg	—	—	—	0.46	3408	1929	[36]
—	—	—	—	0.425	7000	3085	[29]
—	—	—	—	0.56	3590	1980	[35]
—	1.54	3.4	0.6	**0.45**	**3000**	**3200**	
Ca	—	—	—	0.4	3958	1166	[36]
—	—	—	—	0.345	5535	1200	[29]
—	—	—	—	0.49	4180	1210	[35]
—	1.825	4.11	0.91	**0.34**	**4150**	**1700**	
Post-transition metals							
Al	—	—	—	0.64	8000	4470	[35]
—	—	—	—	0.69	7150	5458	[36]
—	—	—	—	0.28	8860	3120	[29]
—	—	—	—	0.47	6890	1782	[34]
—	3.34	2.98	0.63	**0.65**	**7400**	**8500**	
In	—	—	—	2.05	5823	3083	[36]
—	—	—	—	1.1	8560	2725	[29]
—	—	—	—	1.84	6420	2430	[35]
—	2.6	3.47	0.68	**1.8**	**5400**	**4400**	
Ga	—	—	—	1.77	7043	5329	[36]
—	—	—	—	0.735	8880	3150	[29]
—	—	—	—	1.77	7210	4310	[35]
—	2.78	3.164	0.661	**1.38**	**6110**	**5910**	
Transition metals							
Fe	—	—	—	2.03	9600	8250	[35]
—	—	—	—	2.04	9340	10,354	[36]
—	4.29	2.662	0.517	**1.98**	**8950**	**16,500**	
Ni	—	—	—	2.19	10,330	9120	[35]
—	—	—	—	2.3	9600	11,000	[36]
—	4.435	2.605	0.51	**2.2**	**9300**	**18,200**	
Cu	—	—	—	2.33	7600	8300	[36]
—	—	—	—	2.39	8390	7460	[35]
—	—	—	—	1.4	7620	5770	[29]
—	3.5	2.662	0.513	**2.3**	**7250**	**13,500**	
Zn	—	—	—	2.29	3190	2630	[35]
—	—	—	—	2.0	3170	2904	[36]
—	1.35	2.91	0.41	**2.25**	**2120**	**5400**	

Table 2 (continued).

Metal	ΔE, eV	y_0	l_0	ρ_{cr}, g cm^{-3}	T_{cr}, K	P_{cr}, atm	Reference
Zr	—	—	—	1.79	16,250	7520	[35]
—	—	—	—	1.4 ± 0.3	$14{,}500 \pm 1500$	4100	[141]
—	—	—	—	2.24	9660	6674	[33]
—	6.32	3.341	0.746	**1.4**	**14,400**	**10,700**	
Nb	—	—	—	2.59	19,040	12,520	[35]
—	—	—	—	2.02	9989	9630	[120]
—	7.47	3.077	0.63	**2.0**	**16,200**	**17,600**	
Mo	—	—	—	3.18	16,140	12,630	[35]
—	—	—	—	2.62	14,588	11,844	[36]
—	—	—	—	—	$12{,}500 \pm 1000$	$10{,}000 \pm 1000$	[59]
—	6.81	2.926	0.5	**2.8**	**12,870**	**22,400**	
Pd	—	—	—	3.2	10,760	7640	[35]
—	—	—	—	3.06	8300	7085	[36]
—	3.936	2.869	0.447	**3.5**	**6850**	**14,900**	
Cd	—	—	—	2.74	2790	1600	[35]
—	—	—	—	2.33	2619	1615	[36]
—	1.16	3.266	0.4	**3.0**	**1600**	**3600**	
Ta	—	—	—	5.04	20,570	13,500	[35]
—	—	—	—	4.28	17,329	12,223	[36]
—	—	—	—	4.3	12,000	14,000	[29]
—	—	—	—	4.26	9284	9990	[120]
—	—	—	—	4.35	11,600	5000	[63]
—	—	—	—	3.83	13,380	7070	[39]
—	—	—	—	3.32	13,400	—	[142]
—	8.09	3.06	0.62	**4.2**	**17,400**	**18,700**	
Pt	—	—	—	5.02	14,330	8700	[35]
—	—	—	—	5.5	12,526	10,505	[36]
—	—	—	—	4.72	9286	9490	[120]
—	—	—	—	5.08	8970	3880	[122]
—	5.852	2.888	0.447	**6.2**	**10,150**	**22,000**	
Ag	—	—	—	2.93	7010	4500	[35]
—	—	—	—	2.7	6410	4800	[36]
—	—	—	—	2.89	5130	1140	[122]
—	2.96	3.02	0.51	**3.0**	**5500**	**9000**	
Au	—	—	—	5.68	8970	6100	[35]
—	—	—	—	5.0	8267	6265	[36]
—	—	—	—	4.69	6520	1290	[122]
—	—	—	—	7.6 ± 1.5	7400 ± 1100	5300 ± 200	[143]
—	3.78	3.0	0.445	**6.0**	**6250**	**12,900**	

Note. Boldface shows the results our calculations and italics show the experimental data for alkali metals.

meters of the solid state:

$$T_{cr} = \Delta E E^*(a^*_{cr}) \approx 0.2\Delta E. \tag{39}$$

In a sense, the calculations performed can be regarded as the derivation of the Kopp–Lang rule. Transition metals were assigned to a group of their own: for them, $\eta \sim 0.14-0.16$. The resulting relation (39) reveals the physical meaning of Stishov's result and the Kopp–Lang rule: cohesion of less than 1/5 of the evaporation energy does not lead to the vapor–liquid phase transition. The phase transition occurs at temperatures below 1/5 of the vaporization heat. This is exactly the small ('zero') value of cohesion according to Stishov [115].

4.5 Critical pressure

Thermodynamic model (32) yields a somewhat overestimated value of the critical pressure in comparison with experiments with alkali metal vapors. Our attempts to improve model (32) did not lead to noticeable success. By adjusting the pressure, we change the critical density and temperature. In this situation, introducing a phenomenological correction factor to the pressure can be proposed. It turns out to be quite simple. The pressure P^{cr}_{calc} calculated in the framework of model (32) must be multiplied by the factor $(y_0/y_{cr})^3$, the ratio of specific volumes under normal conditions taken at the critical point:

$$P^{cr}_{corr} = P^{cr}_{calc}\left(\frac{y_0}{y_{cr}}\right)^3. \tag{40}$$

The correction introduced in (40) significantly improves the agreement with the critical pressure estimates by other authors for all metals under consideration. The critical density, temperature, and pressure of most metals calculated by formulas (37), (39), and (40) are given in [113].

4.6 Binodal of the vapor–liquid transition

Model (33) allows analytically calculating the binodals of the vapor–liquid phase transition for all considered metals, i.e., calculating the densities of the coexisting liquid and gas phases (saturated vapors). For this, we have to solve the system of balance equations on the binodal, which ensures the equality of chemical potentials and pressures for the liquid and gas phases.

As an example, in Fig. 5 we show the calculated binodal for molybdenum. The critical point parameters estimated by other authors [35, 36, 120–122] are shown along with experimental data on the liquid branch of the binodal [121, 123, 124]. Binodals for other metals (Al, Cu, Fe, Au, W, and Ta) are presented in [113, 116–119].

4.7 Atomic hydrogen

Under normal conditions, hydrogen is a molecular gas. Atomic hydrogen does not exist under natural conditions. In [7], we considered hypothetical hydrogen: purely atomic, without molecules. We obtained a formal expression for the cohesion of hydrogen in Section 3. Using relations of the 1+ model, atomic hydrogen isotherms (7,000–10,000 K) were calculated, which clearly showed in [7] the presence of a first-order phase transition with a characteristic van der Waals loop. The parameters of the critical transition point were determined as $P_{cr} \sim 41{,}000$ atm, $\rho_{cr} \sim 0.1$ g cm^{-3}, and $T_{cr} \sim 9{,}750$ K. This is a transition from an atomic gas to a metalized liquid, because it exhibits cohesion and jellium electrons are present. Indeed, at the transition point, the cold ionization degree is equal to 0.386, which means that almost a half (but not all) of the bound electrons have become metalized. Their number increases exponentially as the density increases. The size of the WS cell at the critical point, expressed in Bohr radii, is $y_{cr} \sim 3$, and hence the atom still exists as a particle. The value of y_{cr} is close to the value $y = 3.65$ at which the binding energy vanishes, in agreement with Stishov's hypothesis [115]. The binding energy is negative. Of course, in real hydrogen under the critical conditions thus found, a large number of molecules are present and such a transition cannot be observed.

We used the atomic–molecular model to calculate the degree of dissociation at the critical point [10]. It turned out to be about 0.2; the gas remains predominantly molecular, 80% of it consisting of molecules. We also calculated the $T = 10{,}000$ K critical isotherm in the density range that includes our new transition, but taking the molecules into account. This transition turned out to occur on the purely atomic branch, being invisible on the atomic–molecular branch, where it is overwhelmed by the contribution of molecules. If any means could be used to destroy the molecules, then compressing atomic hydrogen would allow obtaining liquid metallic hydrogen. At present, methods of shock-wave compression are used to achieve states with solid metallic hydrogen, e.g., by spherical explosive devices or high-power laser radiation.

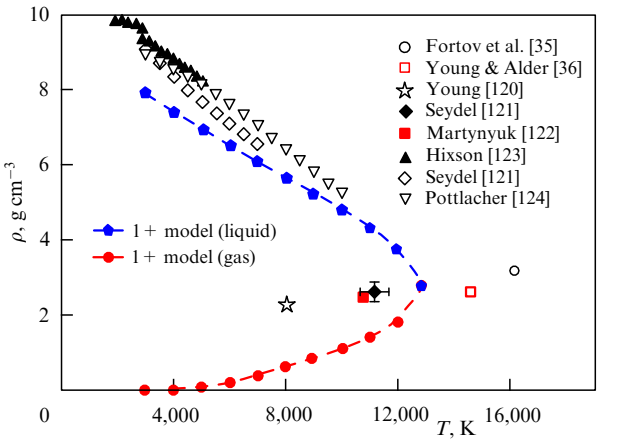

Figure 5. Binodal for molybdenum.

4.8 Excitons

The phase transition of an exciton gas into a liquid phase (condensation into an electron–hole droplet) was predicted by Keldysh [125] and was subsequently revealed experimentally [126]. No generally accepted physical model has been proposed that would allow calculating or estimating the critical parameters of the transition. In the foregoing, we considered the vapor–liquid (insulator–metal) phase transition arising in (hypothetical molecule-free) atomic hydrogen. There is a physical analogy between an exciton and the hydrogen atom, and we therefore used our 'hydrogenic' approach [7] to describe the phase transition in a dense gas of excitons, all the more so because the role of biexcitons (exciton molecules) in the condensation process is believed to be insignificant. We considered a model exciton gas without reference to real semiconductor systems, with the goal of constructing a physical model leading to a phase transition and allowing the critical parameters to be calculated. It turned out that the use of cohesion calculated for an exciton gas gives rise to the vapor–liquid phase transition in the gas of excitons. The use of cohesion allows viewing the liquid phase as a metalized one, containing jellium electrons, which means that the vapor–liquid transition coincides with the insulator–metal transition. The critical parameters and the binodal are in qualitative agreement with observations. The resulting transition is similar in physical nature to the insulator–metal transition in atomic hydrogen and in alkali metal vapors. The absence of thermal ionization of the exciton gas in our model allows us to conclude that this transition is not a plasma phase transition [83].

It is generally accepted [125] that excitons are bound states of an electron and a hole. Excitons differ from hydrogen atoms by the reduced $\mu = cm_e$ and translational $M = 4\mu$ exciton masses, where m_e is the electron mass and c is a numerical coefficient, and by the effective charge $e^* = e/\sqrt{\kappa}$, where e is the electron charge and κ is the dielectric constant. The Schrödinger equation for an exciton is identical to that for a hydrogen atom if we use the 'excitonic' atomic energy units Ry_{ex} and lengths a_0^{ex}:

$$\mathrm{Ry}_{ex} = \frac{\mu e^4}{2\hbar^2\kappa^2} = \mathrm{Ry}\,\frac{\mu}{m_e}\,\frac{1}{\kappa^2}\,, \tag{41}$$

$$a_0^{ex} = \frac{\hbar^2}{\mu e^2}\,\kappa = a_0\,\frac{m_e}{\mu}\,\kappa\,. \tag{42}$$

For hydrogen, cohesion expressed in atomic (hydrogen) units, which we calculated in [7], was discussed in Section 3. We now consider a system of model excitons with the parameters $c = 0.1$ and $\kappa = 10$ [125]. For an exciton gas with the density n^{ex}, using the coincidence of all equations written in dimensionless form for hydrogen and excitons, we obtain the collective binding energy of excitons (cohesion) by simply moving to 'excitonic' atomic units. Naturally, we use the exciton Fermi energy $E_F^{ex} = E_F(m_e/\mu)$ in calculations.

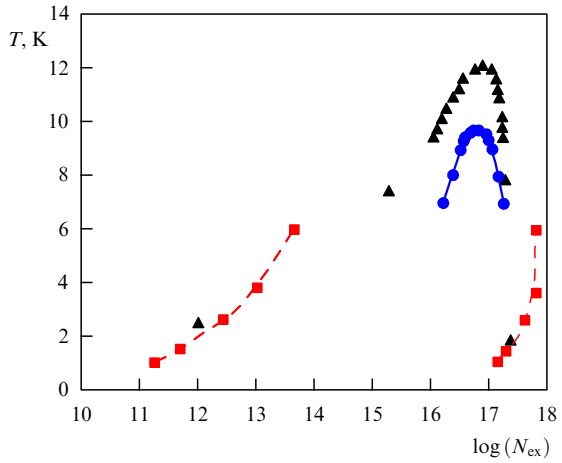

Figure 6. Binodal of exciton gas. Triangles: experiment [126]; squares: data from numerical simulations [83]; dots: 1+ model.

The calculations in [6] show complete similarity of the results for hydrogen and excitons.

A number of qualitative estimates can already be inferred from the calculation of the actual cohesion of excitons. The exciton evaporation energy (the absolute minimum of the cohesion curve) turns out to be of the order of 30 K. A crystalline state of excitons may exist with the normal density $n_0^{\rm ex} \sim 4.5 \times 10^{17}$ cm^{-3} (the coordinate of the minimum $y_0 = 1.53$). Cohesion vanishes at $y \sim 3.65$, which, according to Stishov's hypothesis [115], already at this stage allows estimating the critical density of the vapor–liquid transition as $n_{\rm cr}^{\rm ex} \sim 3.3 \times 10^{16}$ cm^{-3}, which is in qualitative agreement with the experiment. The free energy of a system of $N_{\rm ex}$ excitons placed in a volume V at a temperature T is completely analogous to the one that we used for hydrogen and alkali metal vapors in Section 4 [6]. The constructed exciton gas isotherms for temperatures of 7, 8.5, 9, and 10 K [6] indicate the presence of a phase transition with a characteristic van der Waals loop. The parameters of the critical transition point are easy to estimate: $P_{\rm cr} \sim 42$ dyn cm^{-2}, $n_{\rm cr} \sim 6 \times 10^{16}$ cm^{-3}, and $T_{\rm cr} \sim 10$ K. The transition occurs from the atomic exciton gas into a metalized liquid, because it has a collective binding energy and conduction electrons are present. Solving the system of equations for the balance of chemical potentials and pressures, we obtain the sought values of density, pressure, and temperature along the binodal.

In Fig. 6, we show the calculated binodal of excitons in temperature–density coordinates. We also indicate the experimental data [126] and the results of a numerical calculation by the quantum Monte Carlo method [83] for a model Coulomb system with a plasma phase transition [80]. A fair qualitative agreement between the calculation in [6] and experiment can be seen. We have limited ourself to considering a model exciton system without reference to real semiconductors, setting our main goal as the construction of an exciton gas model with a vapor–liquid phase transition, different from the plasma one.

5. Atomic–molecular fluid, 2+ model

Experiments on shock compression of liquid deuterium and hydrogen have recently been actively discussed in the literature [98–102]. The first experiments [98] revealed a high, even anomalous, compressibility of deuterium, albeit with a significant inaccuracy. The subsequent measurements (on other devices) did not reveal such anomalous degrees of compression [99, 100], but nevertheless uniformly filled a certain region on the PV plane located at a noticeable distance to the left of the experimental region [98]. Among experts, the opinion was expressed that the first experiments were inaccurate and even erroneous. But the authors of [98] did not retract their data. Numerous attempts have been made to explain the results obtained [103]. Importantly for what follows, all theoretical dependences of the pressure on the density on the Hugoniot adiabat, which more or less fit into the domain covered by experiments, are continuous [103]. Only one of these, and quite an exotic one, the 'linear mixture' model by Ross [127], led to the anomalous compressibility corresponding to the data in [98]. In that model, the free energy of hydrogen (or deuterium) was defined as a linear mixture of the atomic–molecular and metallic components, with molar fractions. The atomic–molecular component was described standardly, in the framework of the fluidic perturbation theory for a mixture of atoms and molecules, and the liquid–metal component was described in the approximation of a mixture of degenerate electrons and classical ions. No physical mechanisms for the transformation of one component into another were provided in the model, but their molar densities changed such that their sum was equal to unity. The Ross model is in fact an interpolation between two phases, applicable at the ends of the interpolation interval at low densities (atomic–molecular fluid) or high densities (metalized liquid hydrogen). The shock adiabat calculated in the approximation of a linear Ross mixture [127] was a continuous function of volume and gave high compressibility values, which was related to the dominance of the liquid-metal component at high densities. Thus, the Ross model was the first to associate high compressibility values with the metalization of hydrogen (deuterium).

In [10], we proposed a physical model of metalization of the atomic component of molecular hydrogen under compression via the dissociation of molecules, occurring as a second-order phase transition already mentioned in the Introduction, the dissociative phase transition. The model is based on the assumption that the interaction of free (dissociated) atoms in dense molecular hydrogen becomes collective and is caused by the appearance of jellium electrons and cohesion, just as in the 1+ model considered previously. In a sufficiently dense gas, the collective binding energy of dissociated atoms is comparable to the binding energy of an atom in a molecule (half the dissociation energy), and therefore the dissociation of molecules increases. Preliminary estimates of the critical transition point made in [10] showed that it lies in the vicinity of the anomaly of the Hugoniot adiabat for deuterium.

5.1 Chemical 2+ model of atomic–molecular hydrogen (deuterium)

The free energy of a dissociating atomic–molecular mixture of $N_{\rm m}$ molecules and $N_{\rm a}$ atoms in a volume V at a temperature T, proposed in [10], has the form

$$F = -N_{\rm a} k_{\rm B} T \ln\left(\frac{eVg_{\rm a}}{N_{\rm a}\lambda_{\rm a}^3}\right) - N_{\rm m} k_{\rm B} T \ln\left(\frac{eVg_{\rm m}\Sigma_{\rm m}}{N_{\rm m}\lambda_{\rm m}^3}\right)$$
$$+ (N_{\rm a} + N_{\rm m}) k_{\rm B} T \frac{4\eta - 3\eta^2}{(1-\eta)^2} + \frac{1}{2} N_{\rm a} E_{\rm coh}(y_{\rm a}), \qquad (43)$$

where $\lambda_{a,m} = \sqrt{2\pi\hbar^2/(m_{a,m}k_B T)}$ is the thermal wavelength of an atom or a molecule and $g_{a,m}$ are their statistical weights, Σ_m is the partition function of the molecule, and $E_{coh}(y_a)$ is the collective binding energy of dense atomic hydrogen as a function of the dimensionless radius of the WS atomic cell, expressed in Bohr radii. In this section, we use the expression

$$\eta = \frac{4}{3}\pi\left(\frac{N_a}{V}R_{HSA}^3 + \frac{N_m}{V}R_{HSM}^3\right)$$

for the excluded volume, which is the overall packing parameter expressed through the radii of hard cores of atoms, R_{HSA} and molecules, R_{HSM}. The first three terms in (43) describe a mixture of atoms and molecules in the Carnahan–Starling excluded volume approximation for a mixture of hard spheres, and the last term, the fourth one, describes the interaction energy of atoms. The atomic component is described totally similarly to the case of the 1+ model.

Well-known thermodynamic relations have been used to obtain expressions for the pressure and chemical potentials of atoms and molecules as well as the dissociative balance equation, solving which allows finding the concentrations of atoms and molecules.

5.2 Isotherms and the binodal of the dissociative phase transition

Solving the dissociative balance equation and calculating the equation of state allowed finding and calculating the binodal of the new phase transition [11].

In Fig. 7, the DPT binodal that we found is presented in reduced dimensionless coordinates, where all thermodynamic quantities are divided by their critical values. This representation of the binodal allows comparing it with the van der Waals binodal. The figure demonstrates the fundamental difference between these phase transitions. In the Introduction, we called this transition a dissociative phase transition, and there is every reason to expect anomalies on the compression adiabat of hydrogen (deuterium), which was qualitatively confirmed by calculations [11].

A binodal with a decreasing dependence of the critical pressure on the critical temperature (Fig. 7b) was mentioned already in [80], and was also obtained in [128], where the effect of a hypothetical plasma phase transition on the equation of state of the atomic plasma of inert gases [129] was studied. That the transitions are located close to each other in the model, but not physically, is due to the presence of a DPT in the molecular gas [11] and a plasma phase transition in the atomic inert-gas plasma [129] (not confirmed in later studies, however).

In [11], a fundamentally different interpretation was proposed for the experimental data in [98–102]. The anomaly region is associated with the presence of a two-phase region on the adiabat caused by the DPT, where a molecular fluid (molecular gas with the density of a liquid) and an atomic metalized liquid are present simultaneously. The density in this region is therefore an ill-defined quantity, which leads to a strong scattering of its values [98] in the anomaly region.

6. Atomic fluid with ionization, 3+ model

The 3+ model appeared as a generalization of the 1+ model in which thermal ionization processes were taken into account and, thus, a mixture of thermally ionized electrons, ions, and

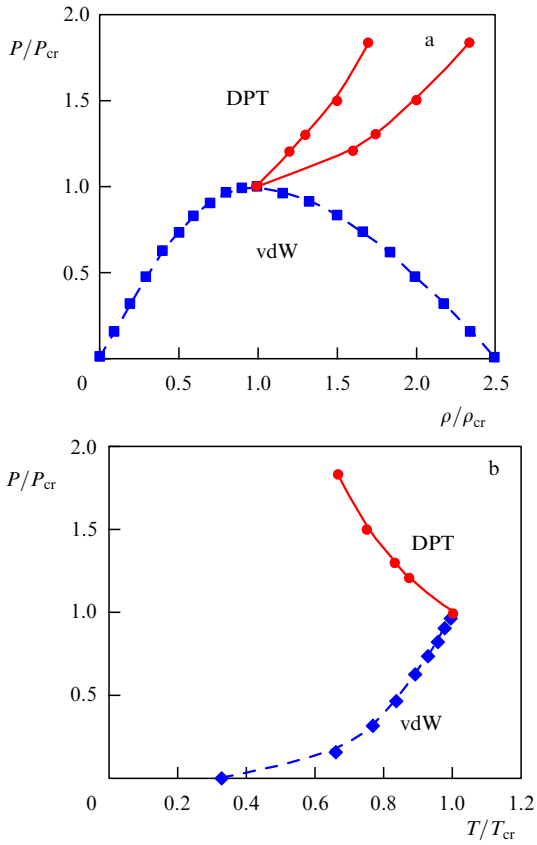

Figure 7. DPT binodal expressed in dimensionless variables (a) pressure–density and (b) pressure–temperature. vdW is the van der Waals binodal, DPT is the dissociative phase transition binodal.

atoms with jellium electrons was considered. The atomic component is described totally similarly to the 1+ model. The charged component, which consists of free thermally ionized electrons and ions, is assumed to be weakly nonideal. The interaction between free charges is described in the nearest-neighbor approximation (NNA) [130, 131], which is justified in a low-temperature plasma at practically any density due to the Boltzmann dominance of attraction. A wide applicability range of the NNA in comparison with the Debye–Hückel approximation was demonstrated in [130]. Jellium electrons are not included as a separate component in the balance equations for the number of particles, because they are part of the electrons bound to atoms. The WS atomic cell is electrically neutral. The 3+ model allows calculating the composition of the gas–plasma mixture, including the concentration of atoms and jellium electrons (the cold ionization degree), as well as the concentration of free thermally ionized electrons and ions. The mutual influence of jellium and thermal electrons and ions is not considered in the first approximation, especially because the domain of their coexistence is small.

The conductivity of dense metal vapors in the 3+ model has two components: the conductivity of thermal electrons, calculated using the Frost formula, and the conductivity of jellium electrons, calculated using the Regel–Ioffe formula. The vapor conductivity changes continuously under compression: starting with the conductivity of thermal electrons, it passes through a minimum and then tends to the conductivity of the jellium. We do not consider multiple thermal ionization, which limits the range of applicability of the model

from the high-temperature side. The decrease in the ionization potential of atoms remains less than the potential itself, and the corrections for the nonideality of free thermally ionized charges are small. The role of Coulomb nonideality increases upon approaching the melting curve, where the effects of degeneracy and the appearance of a long-range order must also be taken into account.

6.1 Helmholtz free energy in the 3+ model

Let us consider a system of N_a atoms, N_e electrons, and N_i ions placed into a volume V at a temperature T. Once again, importantly for what follows, we introduce WS cell radii for the atomic and charged components, $R_a = (3V/4\pi N_a)^{1/3}$ and $R_i = (3V/4\pi N_i)^{1/3}$. For a normal metal, the density is $n_0 = N_0/V$ and the WS cell radius is denoted by R_0. We write the free energy of the system as the sum of the free energies of the atomic and charged components in the additive approximation:

$$F = F_a + F_{ch}\,, \tag{44}$$

where

$$F_a = -N_a k_B T \ln\left(\frac{eVg_a \exp(\beta I)}{N_a \lambda_a^3}\right) + N_a k_B T \frac{4\eta - 3\eta^2}{(1-\eta)^2} + \frac{1}{2} N_a E_{coh}(y_a)\,, \tag{45}$$

$$F_{ch} = -N_e k_B T \ln\left(\frac{eVg_e}{N_e \lambda_e^3}\right) - N_i k_B T \ln\left(\frac{eVg_i}{N_i \lambda_i^3}\right) - (N_e + N_i)\Delta f_{ei}\,. \tag{46}$$

Cross terms related to the atom–charge interaction are not taken into account in the first approximation, because the domain where the concentration of atoms and charges is simultaneously high is not large under the conditions that we assume. The first term in the expression for free energy (44), Eqn (45), is exactly the same as in the 1+ model, Eqn (33); $n_{a,e,i} = N_{a,e,i}/V$ are the densities of the corresponding components; η is the packing parameter; $E_{coh}(y_a)$ is the energy of cohesion, Eqn (22). Knowing the density of atoms, we can determine the density of jellium electrons $n_j = N_j/V$ in terms of the cold ionization degree α_j:

$$n_j = \alpha_j n_a\,. \tag{47}$$

The available methods to calculate α_j were described in Section 2. In what follows, we use the Hartree–Fock method, Eqn (2). The second term in the expression for free energy (44), written in (46), describes the ionized component of the gas–plasma mixture. In (46), λ_e and λ_i are the thermal wavelengths of an electron and an ion, and g_e and g_i are their statistical weights. Without delving into a discussion of the correction for the Coulomb interaction between an electron and an ion, we use the NNA for Δf_{ei} [130, 131]: $\Delta f_{ei} = ce^2/R_i$. We choose the constant such that the energy of interaction of the electron with the nearest ion ($c = 3/4$) is included in the decrease in the ionization potential of the atom.

6.2 Ionization balance equation

The equilibrium composition of a gas–plasma mixture is determined from the solution of balance equations, the leading role among which is played by the relation between the chemical potentials of atoms μ_a, electrons μ_e, and ions μ_i in the ionization reaction:

$$\mu_a = \mu_e + \mu_i\,. \tag{48}$$

Dimensionless ($\beta = 1/k_B T$) chemical potentials are determined from the free energy as $\beta\mu_{a,e,i} = \partial\beta F/\partial N_{a,e,i}$ and are equal to

$$\beta\mu_a = -\ln\frac{Vg_a}{N_a\lambda_a^3} + \mathrm{HS}(\eta) - \frac{\beta E_{coh}}{2}\left(1 - \frac{y_a}{3E_{coh}}\frac{\partial E_{coh}}{\partial y_a}\right), \tag{49}$$

$$\beta\mu_{e,i} = -\ln\frac{Vg_{e,i}}{N_{e,i}\lambda_{e,i}^3} - \frac{2\,\mathrm{Ry}}{y_i}\,, \tag{50}$$

$$\mathrm{HS}(\eta) = \frac{8\eta - 9\eta^2 + 3\eta^3}{(1-\eta)^3}\,. \tag{51}$$

Introducing the thermal ionization degree $\alpha = n_{e,i}/n$, we can use (48) to obtain the ionization balance equation — the Saha formula:

$$\frac{1-\alpha}{\alpha^2} = n\lambda_e^3 \frac{g_a}{2g_i}\exp(\beta I) \times \exp\left[-\frac{2\beta\,\mathrm{Ry}}{y_i} - \frac{\beta E_{coh}}{2}\left(1 - \frac{y_a}{3E_{coh}}\frac{\partial E_{coh}}{\partial y_a}\right) - \mathrm{HS}(\eta)\right]. \tag{52}$$

The Saha formula must be supplemented with the electroneutrality and balance equations

$$n_e = n_i\,, \tag{53}$$

$$n = n_i + n_a\,. \tag{54}$$

Equations (52) and (53), (54) fully determine the composition of the gas–plasma mixture, and Eqn (47) allows finding the density of the new component, the electron jellium. These equations are solved by the dependences $n_{a,e,i}(n)$, which after the use of (47) yield the dependences $n_j(n)$.

6.3 Equation of state

In the 3+ model, using the basic thermodynamic formulas for the pressure $P = -\partial F/\partial V$ and internal energy $E = \partial\beta F/\partial\beta$, we obtain

$$P = n_a k_B T\left(1 + \frac{4-2\eta}{(1-\eta)^3}\,\eta\right) - \frac{1}{2} n_a \frac{y_a}{3}\frac{\partial E_{coh}}{\partial y_a} + (n_e + n_i)k_B T\left(1 - \frac{1}{6}\,c\,\frac{2\beta\,\mathrm{Ry}}{y_i}\right), \tag{55}$$

$$E = \frac{3}{2}\,k_B T(N_a + N_e + N_i) - IN_a + \frac{1}{2}\,N_a E_{coh}(y_a) - N_e c\,\frac{2\,\mathrm{Ry}}{y_i}\,. \tag{56}$$

The choice of the zero level for the energy of metal vapors is discussed in [4].

6.4 Conductivity

Thermally ionized electrons and jellium electrons lie in different energy ranges. The former are in the range of positive energies, sometimes referred to as the continuous spectrum. Jellium electrons have negative energy, but they can move across space. They are separated by an energy close to the ionization potential of an atom. It is natural to assume that their contributions to the total conductivity σ of the gas–plasma mixture are additive:

$$\sigma = \sigma_t + \sigma_j\,. \tag{57}$$

Here, σ_t is the conductivity of thermal electrons and σ_j is the electron conductivity of the jellium. To calculate the conductivity of thermal electrons σ_t, we use a formula that appears in numerous applications and goes under different names in the literature: the τ-approximation [78], the Lorentz–Bloch formula [132], and the Frost formula [133, 134]. All of these are essentially the same and use the Lorentz approximation for the conductivity of a light particle in the medium of heavy ones, with possible corrections for electron–electron collisions, the Fermi–Dirac velocity distribution function of electrons, and the structure factor [132]. The last factor becomes significant only at sufficiently high densities. We use the Lorentz formula, corrected for e−e collisions, with the classical Maxwell distribution function [134], and refer to it as the Frost formula for brevity:

$$\sigma_t = \frac{4\alpha n e^2 \beta^{5/2}}{3\sqrt{2\pi m_e}} \frac{1}{9\times 10^{11}} \times \int_0^\infty \frac{\exp(-\beta\epsilon)\epsilon^{3/2}\,d\epsilon}{\sqrt{\epsilon}\left[(1-\alpha)nQ_{ea}(\epsilon)+\alpha n\gamma_e^{-1}Q_{ei}(\epsilon,\Gamma)\right]}, \quad (58)$$

where ϵ is the energy of a thermal electron, $Q_{ea}(\epsilon)$ is the transport cross section for electron scattering by an atom, $\gamma_e = 0.582$ is the Spitzer factor, $Q_{ei}(\epsilon,\Gamma)$ is the Rutherford transport scattering cross section for an electron on an ion, and $\Gamma = \beta e^2\sqrt{4\pi\beta e^2(n_e+n_i)}$ is the Coulomb nonideality parameter, equal to the ratio of the Debye energy to the temperature.

For the cross sections of electron scattering by an atom and an ion, we take the relations that we used previously in the ion–molecular chemical model of metal vapor plasma [135]:

$$Q_{ea}(\epsilon) = \frac{\pi^2\sqrt{3}}{2}\sqrt{P_a}a_0^2\sqrt{\frac{\mathrm{Ry}}{\epsilon}}, \quad (59)$$

$$Q_{ei}(\epsilon,\Gamma) = 4\pi a_0^2\left(\frac{\mathrm{Ry}}{\epsilon}\right)^2 \ln\left(1+\frac{3\sqrt{2}}{\Gamma}\right). \quad (60)$$

In (59), P_a is the polarizability of an atom expressed in atomic units [136].

Jellium electrons also participate in conductivity, because they can move from cell to cell, and their conductivity is determined by formula (8) (see Section 2).

7. Thermal and electrophysical properties of the dense plasma of metal vapors. Comparison with experimental and numerical simulation results

7.1 Conductivity of metal vapors on supercritical isotherms

In experimental studies [49–52] of the pulsed explosion of wires placed in glass capillaries, the dependence of the conductivity on density was measured for metal vapors (Al, Cu, Ni, Fe, and W). The measurements covered a wide range of densities, from gas to metal densities under normal conditions. The equation of state was not measured, and the temperature was reconstructed using the SESAME equation of state. In [5], the results of the analysis and processing of experimental data are presented in the form of isotherms.

In the 3+ model framework, we calculated the conductivity of metal vapors on isotherms in the range $T = 8{,}000$–$30{,}000$ K for Al, Cu, Ni, and Fe. Figure 8 shows the results

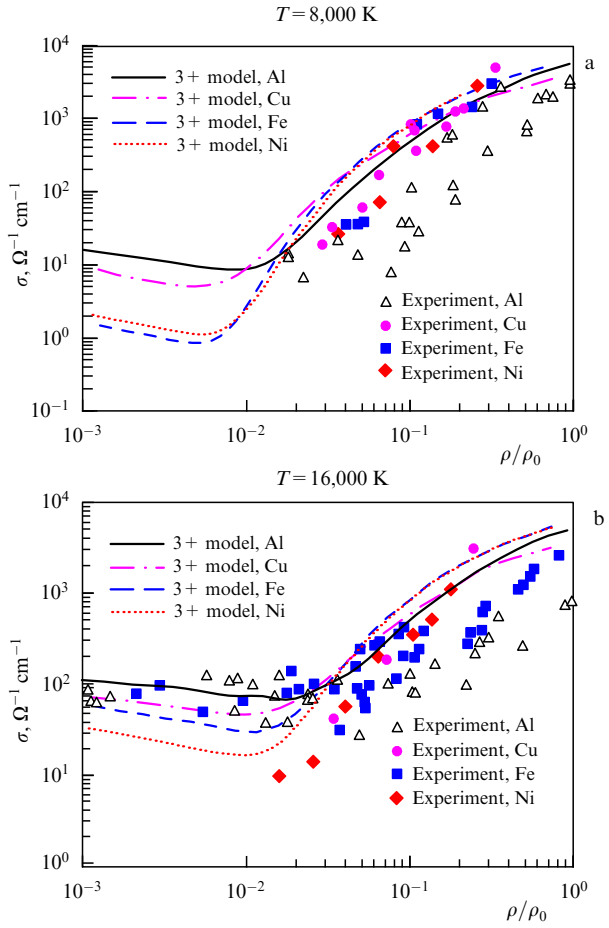

Figure 8. Conductivity of metal vapors at (a) $T = 8{,}000$ K and (b) $T = 16{,}000$ K. Experiment [5]: open triangles, Al; dots, Cu; solid squares, Fe; solid diamonds, Ni. Theory: solid, dashed-dotted, dotted, and dashed lines, respectively, show the results of 3+ model calculations with the jellium electron concentration taken into account in accordance with Hartree–Fock approximation (2) for Al, Cu, Ni, and Fe.

of calculations for the $T = 8{,}000$ K (near-critical) and $T = 16{,}000$ K isotherms. The results of calculations of the conductivity of metals (Al, Cu, Fe, Ni, and Be) on isotherms are presented in more detail in [133, 137].

The results of calculations of the conductivity on different isotherms for aluminum and beryllium are shown in Figs 9 and 10 in comparison with the data of numerical *ab initio* calculations by the QMD method [60, 67]. Calculations based on the proposed model demonstrate a reasonably good agreement with the results of numerical calculations. All calculations (see Figs 8–10) demonstrate an interesting physical effect of the change in the type of charge carriers as metal vapors are compressed. At low densities, the transfer is effected by thermal electrons, as in conventional partly ionized plasmas. As the density increases, solid-state effects start manifesting themselves: a noticeable number of jellium electrons appears. The temperature dependence of the conductivity practically disappears, and the dependence on the density becomes exponential within a certain interval. Comparison with the results of experiments and numerical simulations can serve as a substantiation of our hypothesis on the existence of electron jellium in the gas–plasma domain and its coexistence with electrons of traditional thermal ionization.

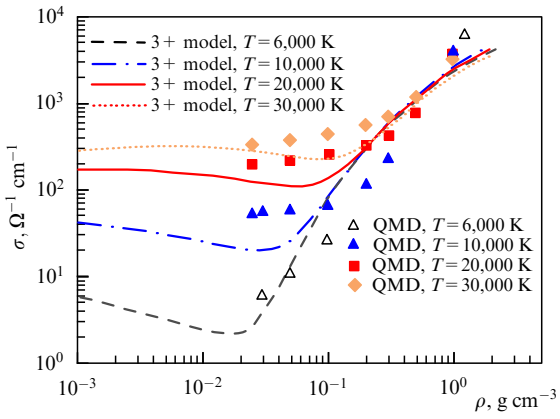

Figure 9. Dependence of the conductivity of aluminum vapors on density along different isotherms. QMD results [60]: open triangles, $T = 6{,}000$ K; solid triangles, $T = 10{,}000$ K; solid squares, $T = 20{,}000$ K; solid diamonds, $T = 30{,}000$ K. Theory: dashed, dashed-dotted, solid, and dotted lines correspond to 3+ model calculations for isotherms $T = 6{,}000$, 10,000, 20,000, and 30,000 K.

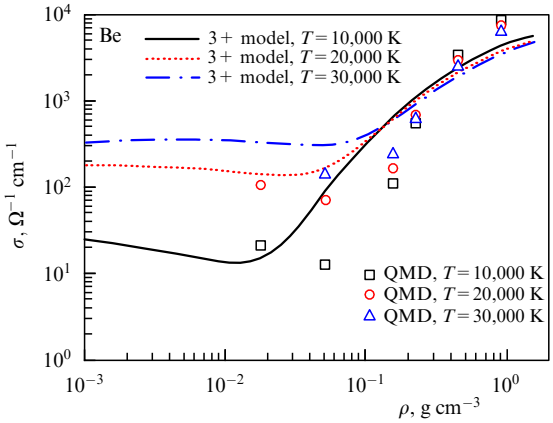

Figure 10. Dependence of beryllium vapor conductivity on density along different isotherms. QMD results [67]: symbols correspond to isotherms $T = 10{,}000$, 20,000, and 30,000 K. Theory: solid, dotted, and dashed-dotted lines show the results of calculations in the 3+ model with the respective isotherms $T = 10{,}000$, 20,000, and 30,000 K.

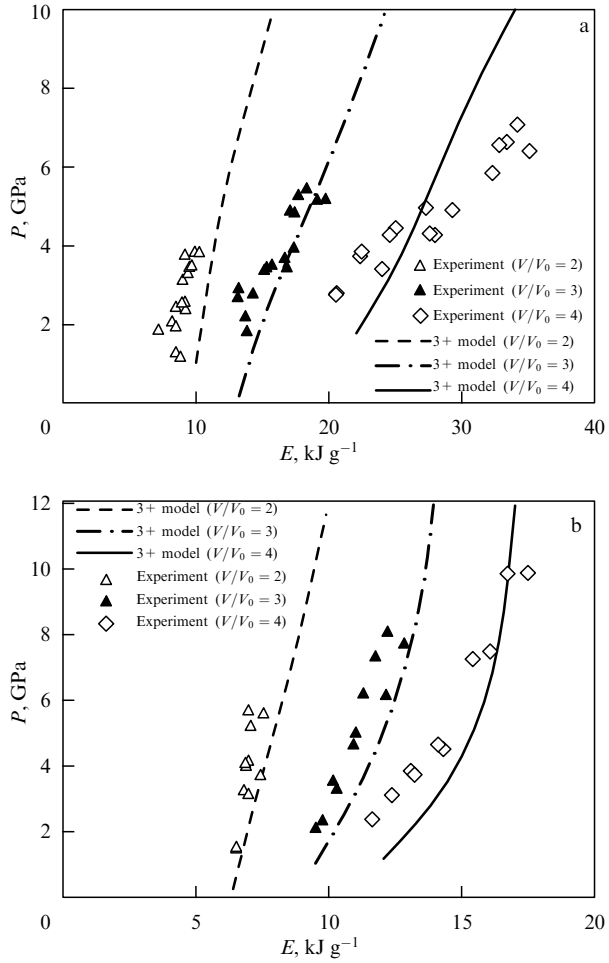

Figure 11. Dependence of pressure on the internal energy for (a) aluminum and (b) jellium along the isochores $V/V_0 = 2$, 3, and 4. Experiment [53, 55]: symbols correspond to the isochores $V/V_0 = 2$, 3, and 4. Theory: dashed, dashed-dotted, and solid lines, respectively, show the results of 3+ model calculations for the isochores $V/V_0 = 2$, 3, and 4.

7.2 Caloric and thermal equations of state of metal vapors

In [53, 55–57], the equation of state and the conductivity were studied simultaneously for a dense plasma of Al, Fe, and Pb vapors using installations for the electric explosion of foils sandwiched between sapphire plates. The dependences of pressure and conductivity on the internal energy were measured at different isochores: $V/V_0 = 9$, 5.4, 4, 2.7, and 1.93, where $V_0 = 1/\rho_0$ is the volume of the metal under normal conditions. In parallel, the full set of quantities — pressure, internal energy, conductivity, and temperature — was calculated under the same conditions by the numerical method using the VASP package. This allowed the results of a physical experiment, for example, for aluminum, to be supplemented with temperature data.

Figure 11 shows the dependence of the pressure on internal energy at various isochores for aluminum (Fig. 11a) and iron (Fig. 11b). Experimental data [53, 55] and 3+ model calculations are shown. For beryllium, experimental data in the supercritical fluid domain are absent due to the high toxicity of this metal. In [67, 68], the VASP package was used to calculate the properties of beryllium in a wide range of densities and temperatures; the thermal and caloric equations of state were obtained and the conductivity in direct and alternating currents was calculated. The Kubo–Greenwood formalism was used to calculate the conductivity.

In Figs 12 and 13, we show a comparison of our calculations with the results of numerical calculations; an even better agreement between them is observed for the thermal equation of state than for the caloric one. Figure 13 shows the origination of the van der Waals loop for both QMD calculations and the 3+ model, which is indicative of the closeness to the critical point. At high temperatures ($T > 30{,}000$ K), a difference between the 3+ model calculations and numerical calculations is observed, which is associated with the double ionization effect.

7.3 Conductivity (resistance) of supercritical vapors of metals on isochores

Figure 14 shows the results of calculations of the resistance of supercritical aluminum plasma in comparison with the results of a physical and a numerical experiment. Calculations of the conductivity based on the 3+ model describe the experimental data and numerical calculations well. On the chosen isochores, a weak temperature dependence of the conductivity at high compressions is observed [4].

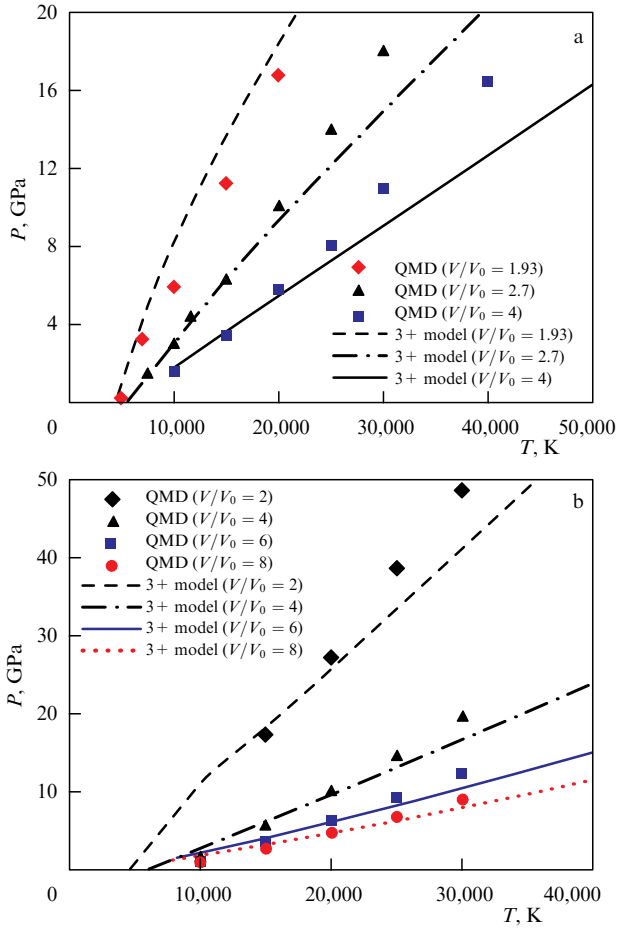

Figure 12. Dependence of pressure on temperature for (a) aluminum and (b) beryllium on isochores. (a) QMD results [60]: symbols correspond to isochores $V/V_0 = 2$, 2.7, and 4. Theory: dashed, dashed-dotted, and solid lines are the results of 3+ model calculations for the respective isochores $V/V_0 = 2$, 2.7, and 4. (b) QMD results [67]: symbols correspond to isochores $V/V_0 = 2$, 4, 6, and 8; dashed, dashed-dotted, solid, and dotted lines, respectively, show the results of 3+ model calculations for the isochores $V/V_0 = 2$, 4, 6, and 8.

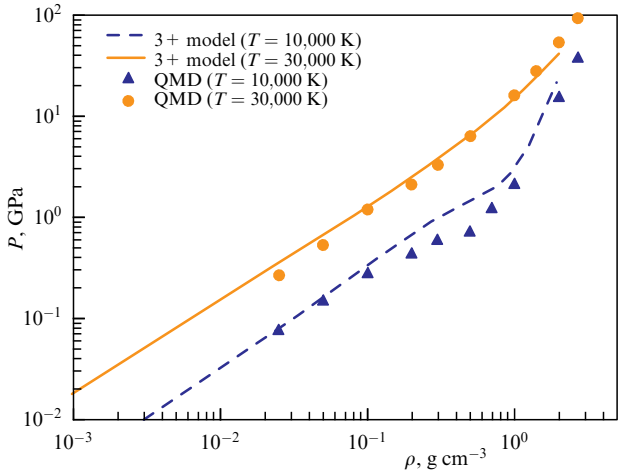

Figure 13. Pressure of aluminum vapors on isotherms. QMD results [61]: symbols correspond to isotherms $T = 10{,}000$ and 30,000 K. Theory: dashed and solid lines, respectively, show the 3+ model results at $T = 10{,}000$ and 30,000 K.

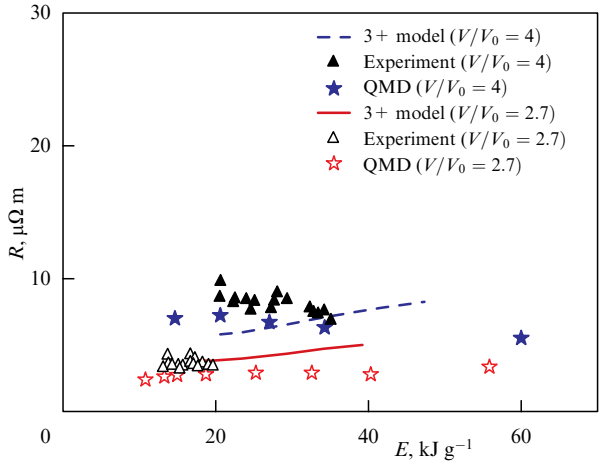

Figure 14. Dependence of the resistance of aluminum vapors on the internal energy for isochores $V/V_0 = 4$ and 2.7. Experiment [53]: filled triangles, $V/V_0 = 4$ [51]; unfilled triangles, $V/V_0 = 2.7$. QMD calculations [53]: filled stars, $V/V_0 = 4$; unfilled stars, $V/V_0 = 2.7$. Theory: dashed and solid lines show the total resistance in the 3+ model framework for the isochores $V/V_0 = 4$ and $V/V_0 = 2.7$.

8. Details of calculations of the conductivity of supercritical inert-gas plasmas

Inert gases are fundamentally different from metal vapors. They are insulators in the gaseous state, and remain so when cooled and compressed to the liquid and solid states. According to the Lennard-Jones–Devonshire theory [138], the collective binding energy is due to the pairwise additive interaction of a test atom with its close environment of the first coordination spheres. The use of the Lennard-Jones potential to calculate the binding energy leads to good results in the framework of classical statistical physics [103]. Using our technique (2) to calculate the electron jellium density leads to the emergence of jellium under compression for inert gases as well. But the jellium that forms must be considered dielectric, because it arises from a completely filled electron shell. The jellium electrons do not directly contribute to the conductivity and the collective binding energy of atoms. In inert gases, the jellium is formed from the tails of the electron density of bound states, and its position on the energy axis is immediately adjacent to the ground level. In [9], we proposed a new effect, unusual for plasma physics, associated with the broadening of the ground level of an atom due to the formation of electron jellium. The appearance of such broadening facilitates thermal ionization, bringing the energy of the ground state of a bound electron closer to the continuum, resulting in a kind of decrease in the ionization potential, but on the other side of the energy scale.

8.1 Ionization balance equation for a dense plasma of inert gases

To calculate the concentrations of components and the dependence of conductivity on density along isotherms, we need the ionization balance equation. We use a version of this equation obtained for the 3+ model (52) with the modification that takes the new role of electron jellium into account:

$$\frac{1-\alpha}{\alpha^2} = n\lambda_e^3 \frac{g_a}{2g_i} \exp\left(\beta I_{\text{eff}}\right). \tag{61}$$

The effective ionization potential of an atom I_{eff} is expressed in terms of the ionization potential I of an isolated atom and

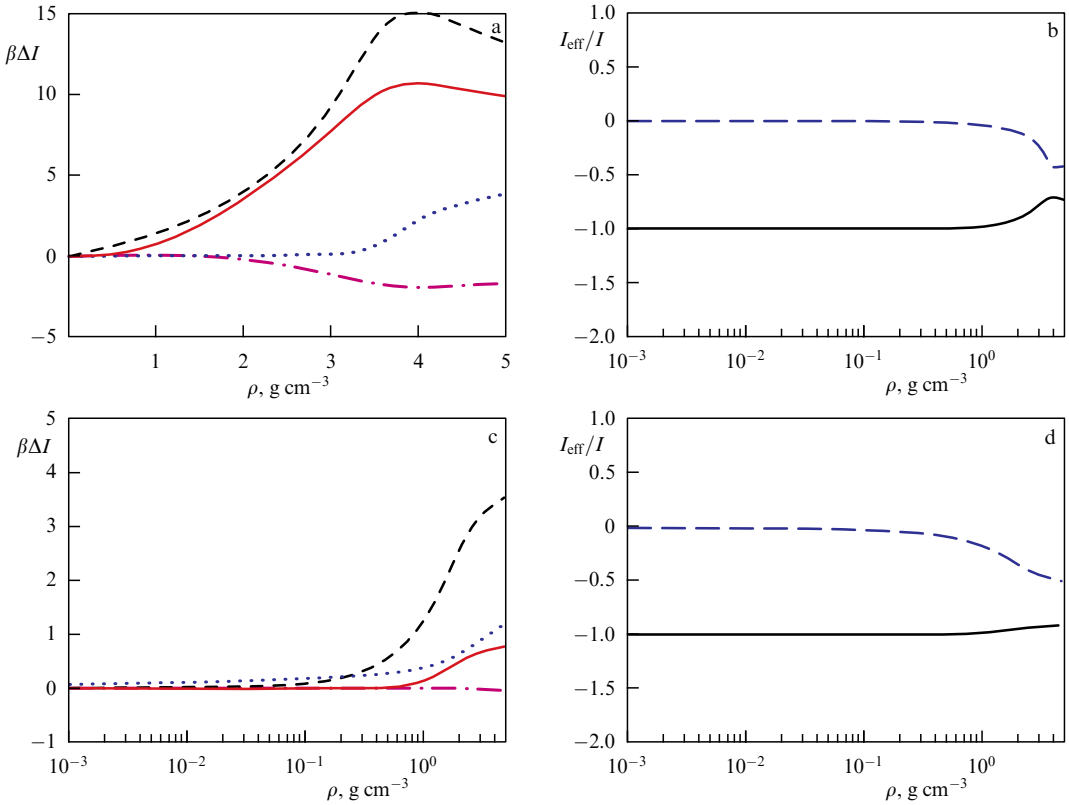

Figure 15. Decrease in atom ionization potential expressed in temperature units for argon plasma at (a, b) $T = 5{,}000$ K and (c, d) 20,000 K as a function of density. (a, c) Contributions of individual components to the decrease in the ionization potential: dotted line (ΔI_{coul}), dashed-dotted line (ΔI_{coll}), dashed line (ΔI_{HS}), red solid line (ΔI_{Fermi}). (b, d) Position of the continuum and ground state expressed in units of the binding energy of an isolated atom. Dashed line: the continuum including the decrease in the ionization potential due to the interaction of particles in the continuous spectrum; solid line: position of the ground state with the Fermi jellium energy taken into account.

its change ΔI due to interaction effects,

$$I_{\text{eff}} = I + \Delta I\,. \tag{62}$$

As the terms making up ΔI, we take the same set as for metal vapors (52), changing it slightly for inert gas plasmas:

$$\Delta I = \Delta I_{\text{coul}} + \Delta I_{\text{coll}} + \Delta I_{\text{HS}} + \Delta I_{\text{Fermi}}\,. \tag{63}$$

The first three terms are almost identical to those in (52). The second term in (63), due to the collective interaction of atoms, is also formally unchanged, but it should be borne in mind in calculations that the nature of the cohesion forces in inert gases is different from that in metal vapors, although they are still described using UBER [47, 48]. The critical parameters calculated using the 1+ model for inert gases give values close to the experimental ones [117]. The third term describes the contribution of the excluded volume and is traditionally described using the Carnahan–Starling formula for the hard-sphere model. When calculating the packing parameter $\eta = 4\pi n_{\text{a}} R_{\eta}^3/3$, we use $R_{\eta} = cR_{\text{HS}}$, with the parameter c selected from a comparison with experiment. It turns out to be ~ 0.7–0.8 for all inert gases under consideration. The fourth term, a new one, describes a decrease in the ionization potential of an atom by the amount $E_{\text{Fermi}}(n_{\text{j}}) = (\hbar^2/2m_{\text{e}})(3\pi^2 n_{\text{j}})^{2/3}$ due to the formation of dielectric jellium. In dimensionless variables, it has the form

$$\Delta I_{\text{Fermi}} = -\text{Ry}\,\frac{9\pi}{4}\left(\frac{\alpha_{\text{j}}}{y_{\text{a}}^3}\right)^{2/3}. \tag{64}$$

Solving the Saha equation allows finding the dependence of the thermal ionization degree α on the density n and temperature T. The cold ionization degree α_{j} is included as an intermediate parameter and is related to the concentration of atoms n_{a}.

8.2 Decrease in the ionization potential

Figure 15 shows the results of calculating the terms responsible for the decrease in the ionization potential of an atom in argon plasma. At $T = 5{,}000$ K (Fig. 15a), the leading components are ΔI_{HS} and ΔI_{Fermi}. As the density increases, the Coulomb attraction and collective cohesion forces become noticeable (they slightly cancel each other). The continuum and the ground state coming closer to each other (Fig. 15b) is the reason behind the sharp increase in the concentration of thermally ionized (free) electrons. As the temperature increases (Fig. 15c, d), the role of jellium decreases due to an increase in the ionization degree. The repulsion of the cores and the Coulomb interaction of free charges come to the foreground. The band gap (ground level plus jellium) and the conduction band (continuum) coming closer to each other is similar to the effect leading to the Mott transition in semiconductors.

8.3 Conductivity. Discussion of results

To calculate the conductivity of thermal electrons σ_{t}, we use Frost formula (58). The transport cross sections for the scattering of electrons by inert gas atoms are known experimentally, and their analytic approximations can be found, e.g., in [134]. In Fig. 16, we show the results of calculating the conductivity isotherms of argon plasma in accordance with the 3+ model and the Saha model [8]; experimental data [85, 88] are also presented that demon-

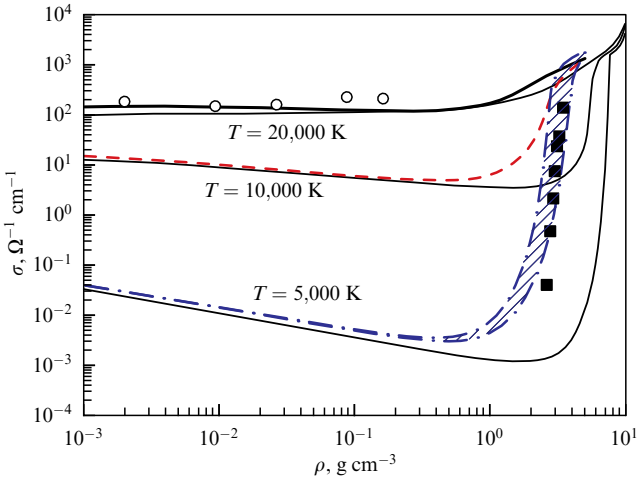

Figure 16. Conductivity of argon plasma. Experiment: circles, the results in [88]; solid squares, [85]. Theory: thin black lines show the results of calculations with the Saha code [8]; dashed-dotted, dashed, and thick solid lines correspond to the 3+ model calculation at the respective temperatures T = 5,000, 10,000, and 20,000 K (c = 0.7). Hatched region corresponds to the calculation at T = 5,000 K for coefficient c = 0.7–0.8.

strate a general regularity: segregation into two groups, which can be conventionally called 'high-temperature' and 'low-temperature.' This is due to different initial states prior to compression: gaseous [88] and condensed [85]. The segregation can be seen especially well for argon plasma. The 'high-temperature' data are almost horizontal and weakly depend on density. The 'low-temperature' data are nearly vertical, which is typical for exponential dependences. The thin solid line in Figure 16 shows the best theoretical calculations by the well-known Saha code [8] at the time of the beginning of this study. They describe the high-temperature data quite satisfactorily and qualitatively describe the low-temperature data.

All the calculations done for Ar, Kr, and Xe are similar. The calculation using the Saha code [8] demonstrates an increase in the conductivity under compression, but only at higher densities lying to the right of the domain of the conductivity increase observed in experiment. The main factor underlying the increase in the conductivity of thermal electrons in the Saha code is the effect of interatomic repulsion, both direct, due to corrections to the free energy in the approximation of either hard or soft spheres, and indirect, due to the deformation of bound levels of an atom in the bounded atom approximation. The crucial factor in our model is the broadening of the ground state due to the Fermi energy of the jellium. The parameters of the appearance of the metalization effect in inert gases do not coincide with the parameters of the vapor–liquid transition, but strongly resemble the Mott transition in semiconductors by their origin and jump-like nature.

9. Gaseous metal and features of vapor–liquid and insulator–metal transitions in metal vapors

In the model of the metal–insulator transition in metal vapors proposed by Likal'ter [28], a new concept of a gaseous metal was introduced, whose possible (albeit hypothetical) existence was already mentioned in [1]. A gaseous Likal'ter metal is a gas of atoms with overlapping regions that are classically accessible to the motion of bound electrons. If such a state is assumed to exist, then the vapor–liquid phase transition is a transition of a metal in a liquid state to the state of a gaseous metal, which is by no means an insulator one. The insulator state of vapors, according to Likal'ter, arises only at high rarefaction. To be precise, the metal–insulator transition does not occur in the vicinity of the critical point. A popular but not yet experimentally confirmed model of the transition is based on the hypothesis of a plasma phase transition. It is argued that, near the binodal of the vapor–liquid transition in the gas–plasma region, an insulator–metal transition occurs due to a jump-like increase in the electron concentration caused by a decrease in the ionization potential of the atom due to the Coulomb interaction [75, 80].

Using the 3+ model, we investigated a number of properties of the new plasma state — a gaseous metal — and discussed its role in the vapor–liquid and insulator–metal transitions in metal vapors. In many aspects, the proposed model is based on Likal'ter's ideas [28] but is not limited to them. The proposed model of a gaseous metal (in contrast to Likal'ter's model) is based on the concept of electron jellium arising under the compression of an atomic gas. The cold ionization degree for various metals (Be, Al, and Cs) is shown in Fig. 2. We believe that the ionic cores bound together by the electron jellium form a gaseous metal, which formally exists at any density and is quite different in that respect from the gaseous metal in the Likal'ter model, moving into it only at a sufficiently high density. It is into a gaseous metal state, rather than an insulator state, that the transition from a liquid metal state occurs under rarefaction. When a gaseous metal is compressed in the gaseous phase at supercritical temperatures, a smooth transition occurs to a state with a metallic level of conductivity.

9.1 Range of existence of a gaseous metal

We jointly consider both ionization processes, thermal and cold, and compare them in order to identify the regions on the phase diagram where one of them dominates. Figure 17 shows the results of calculations of the thermal (α) and cold (α_j) ionization degrees depending on the density on aluminum isotherms. The curves have two intersection points, at low and high densities. At low densities, thermal ionization is high, the atoms are few, and hence the concentration of jellium electrons is low: $\alpha > \alpha_j$. As the density increases, the number of atoms increases, and the jellium density increases with it. Simultaneously, the fraction of thermally ionized electrons decreases, $\alpha < \alpha_j$. With a further increase in density, the effect of a decrease in the ionization potential starts manifesting itself, mostly due to the Coulomb interaction. This leads to an increase in the concentration of thermally ionized electrons and a decrease in the concentration of jellium electrons due to a decrease in the number of atoms.

As the temperature increases, the effect of the intersection of the ionization curves disappears and thermal ionization becomes the predominant ionization mechanism. The critical temperature for aluminum (without the intersection effect) is T_j = 18,000 K. In Fig. 18, we show the aluminum binodal calculated in [116], along with the available experimental data and estimates of the critical point made by different research groups [35, 36]. We also plot the curve corresponding to the two roots of the equation $\alpha = \alpha_j$. The region between the binodal and the curve that we found can be called the region with a mostly cold ionization mechanism. Arguably, this is the region where the plasma is in the state of a gaseous metal;

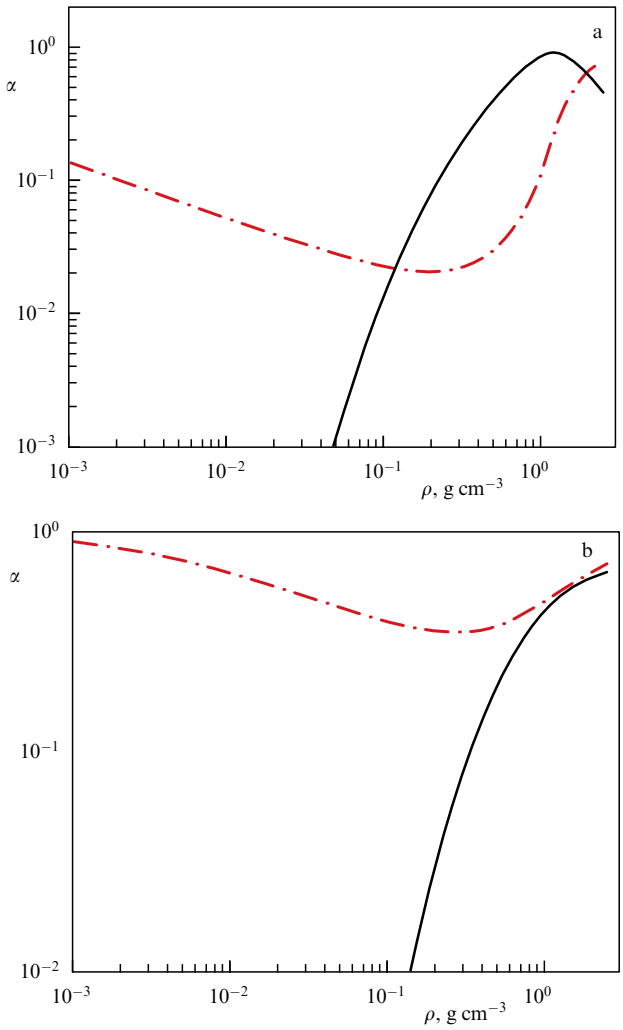

Figure 17. Thermal (dashed-dotted line) and cold (solid line) ionization degrees for Al on isotherms: (a) $T = 8{,}000$ K (near-critical); (b) $T = 18{,}000$ K.

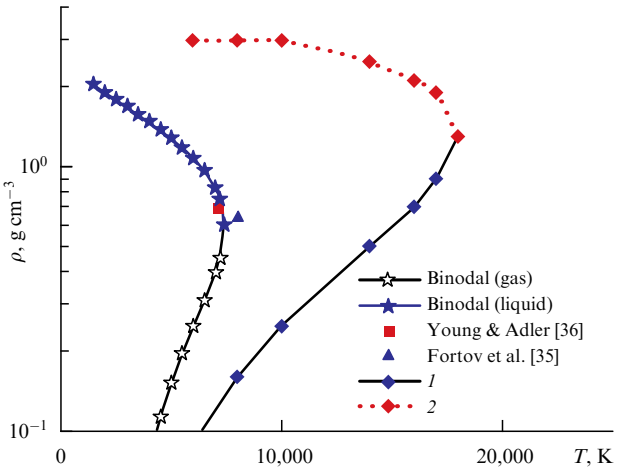

Figure 18. Neighborhood of the binodal for aluminum. Solid line with stars corresponds to the binodal calculated in [116]. For the solid and dotted lines with diamonds (*1* and *2*), the thermal ionization degree is equal to the cold ionization degree.

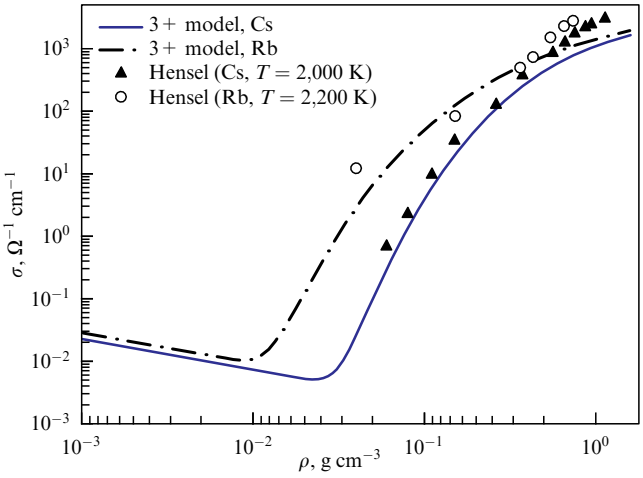

Figure 19. Conductivity of alkali metal vapors on near-critical isotherms as a function of density. Experiment [14]: symbols correspond to the data for Cs and Rb. Theory: solid and dashed-dotted lines, respectively, show calculation results in the 3+ model for Cs and Rb.

although jellium electrons are also present outside the designated area, they are few there. The concentration of conduction electrons within the found area is not determined by the Saha formula.

9.2 Conductivity in the near-critical domain

Most comprehensive measurements of thermodynamic functions and conductivity have been made for Cs and Rb. The binodals of the vapor–liquid transition and the conductivity on the binodal have been measured. This set of experimental data allows using the 3+ model to calculate the conductivity of cesium on the entire binodal [139] using the experimentally obtained density and temperature values. In Fig. 19, we show the result of calculations of the conductivity of Cs and Rb vapors on near-critical isotherms. The jellium electrons make the main contribution to the conductivity. The thermal ionization degree is low. We note the minimum of the conductivity isotherm obtained in the calculations, which we discuss below.

9.3 Minimum of the metal vapor conductivity on isotherms

We have already noted the minimum on the conductivity isotherms, which is to be discussed separately because this effect is characteristic of a gaseous metal, and electron jellium is responsible for this minimum. The presence of the minimum is qualitatively confirmed by our calculations of the conductivity isotherms of various metals [133, 137], numerical simulations, and experiment (see Figs 8–10). At low densities, we have a fully ionized plasma with a weak logarithmic dependence of the conductivity on density. As the density increases, the conductivity decreases, and an increase in the number of atoms leads to an increase in the cold ionization degree. The conductivity is determined by the jellium electrons, and it grows exponentially as the density increases. For high-temperature isotherms, the minimum practically disappears due to the ionization of atoms and the disappearance of the jellium.

9.4 Asymptotic behavior of conductivity isotherms with increasing density

As the density increases, all isotherms reach a 'common' asymptotic regime. The isotherms practically merge, and the conductivity at these densities ceases to depend on the temperature. We noted this property previously [133]. In Figs 20 and 21, we show the calculated conductivity

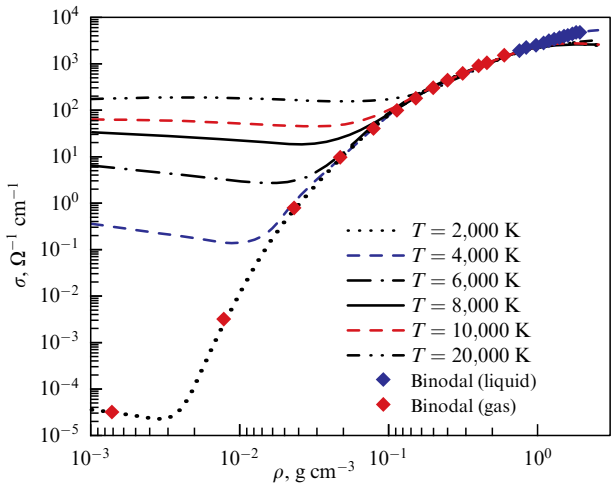

Figure 20. Conductivity of aluminum on isotherms and on the binodal. Lines from bottom up: $T = 2{,}000$, 4,000, 6,000, 8,000, 10,000, and 20,000 K. Diamonds correspond to the conductivity on the binodal that we calculated (see Fig. 18).

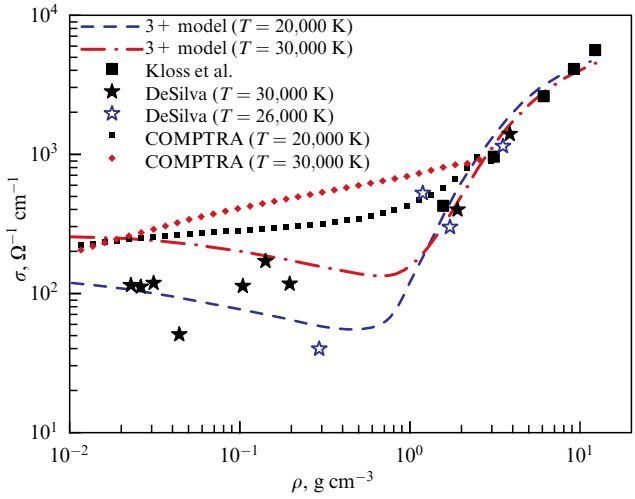

Figure 21. Conductivity of tungsten as a function of density on isotherms. Experiment: unfilled and filled stars, respectively, show results in [5] at $T = 26{,}000$ and 30,000 K; solid squares, results in [140]. Theory: small squares and diamonds, calculation with the COMPTRA code [75] at $T = 20{,}000$ and 30,000 K; dashed and dashed-dotted lines correspond to the 3+ model calculation at $T = 20{,}000$ and 30,000 K.

isotherms and the vapor conductivity on the binodal, both calculated (see Fig. 20) and experimental (see Fig. 21). Surprisingly, the asymptotic behavior of the conductivity coincides with the conductivity calculated along the binodal. In Figure 21, in addition to our calculations within the 3+ model, calculations using the COMPTRA code are plotted [75], allowing the presence of a plasma phase transition. Our calculations are in good agreement with the experiment in [140] on measuring the conductivity of tungsten vapor at the binodal.

Analytic calculations of the conductivity according to the 3+ model for Al and Be (see Figs 9 and 10) and the results of numerical simulations [60, 67] are in fairly good agreement with each other and demonstrate two effects discussed above: the presence of a conductivity minimum and the asymptotic merger of isotherms. The gaseous metal model was originally proposed to work in the vicinity of the critical point [28], but turned out to be successful in a wider range of parameters [139]. We repeat that two hypotheses, both of a solid-state origin, underlie the concept of a gaseous metal: the presence of electron jellium (a seed of the conduction band) and the cohesive, collective interaction of atoms, with the jellium electrons playing an essential role in its formation [114].

10. Conclusion

We have discussed the regularities of the vapor–liquid phase transition and the metalization processes occurring in supercritical metal vapor fluids, atomic and atomic–molecular hydrogen, inert gases, and exciton gas.

Using the proposed models, we calculated the parameters of the critical points and binodals of most metals in the Mendeleev periodic table, including alkali metals, hydrogen, and excitons. Useful relations between solid-state parameters and the critical point parameters have been established. Calculations were done and the results were compared with the results of physical and numerical experiments for the thermal and caloric equations of state for metal vapors. Calculations were done and a comparison was made with the existing experiments for conductivity at the critical points and on the binodal and on near-critical isotherms, taking the cold and thermal ionization processes into account. A model of jump-like metalization of inert gases under compression was proposed. A dissociative phase transition in partly dissociated molecular hydrogen (deuterium) was discovered and described. The region of the existence of a gaseous metal near the binodal was investigated. An interpretation was proposed for the presence of a minimum and the asymptotic behavior of metal vapor conductivity along supercritical isotherms.

We established that, generally speaking, the metal–insulator phase transition in the substances under consideration does not occur in and of itself, because the gas phase, especially near the critical point, contains electron jellium — a seed of the conduction band — and is not a pure insulator. Liquid metal coexists with gaseous metal. We can confidently speak about the existence of a metalization effect under compression, associated with the formation of electron jellium. For a plasma of inert gases, the jump-like metalization effect occurs far from the critical point and can be regarded as being similar to the Mott effect. We concluded that the concept of an 'isolated atom,' which is widely used in statistical physics of gases and plasmas, has to be corrected and is inapplicable to the description of dense gas–plasma states of matter.

This study was done with financial support from the Russian Foundation for Basic Research in the framework of the research project Ekspansia, no. 19-18-50188.

References

1. Zeldovich Ya B, Landau L D *Zh. Eksp. Teor. Fiz.* **14** 32 (1944); Landau L D, Zeldovich Ya B *Acta Physicochim. USSR* **18** 194 (1943)
2. Brazhkin V V et al. *Phys. Usp.* **55** 1061 (2012); *Usp. Fiz. Nauk* **182** 1137 (2012)
3. Brazhkin V V *Phys. Usp.* **60** 954 (2017); *Usp. Fiz. Nauk* **187** 1028 (2017)
4. Khomkin A L, Shumikhin A S *J. Exp. Theor. Phys.* **125** 1189 (2017); *Zh. Eksp. Teor. Fiz.* **152** 1393 (2017)
5. DeSilva A W, Rakhel A D *Contrib. Plasma Phys.* **45** 236 (2005)
6. Khomkin A L, Shumikhin A S *J. Exp. Theor. Phys.* **120** 672 (2015); *Zh. Eksp. Teor. Fiz.* **147** 775 (2015)

7. Khomkin A L, Shumikhin A S *Plasma Phys. Rep.* **39** 857 (2013); *Fiz. Plazmy* **39** 958 (2013)
8. Fortov V E et al. *J. Exp. Theor. Phys.* **97** 259 (2003); *Zh. Eksp. Teor. Fiz.* **124** 288 (2003)
9. Khomkin A L, Shumikhin A S *J. Exp. Theor. Phys.* **128** 739 (2019); *Zh. Eksp. Teor. Fiz.* **155** 869 (2019)
10. Khomkin A L, Shumikhin A S *J. Exp. Theor. Phys.* **114** 89 (2012); *Zh. Eksp. Teor. Fiz.* **141** 101 (2012)
11. Khomkin A L, Shumikhin A S *J. Exp. Theor. Phys.* **119** 453 (2014); *Zh. Eksp. Teor. Fiz.* **146** 518 (2014)
12. Renkert H, Hensel F, Franck E U *Ber. Bunsenges. Phys. Chem.* **75** 507 (1971)
13. Jüngst S, Knuth B, Hensel F *Phys. Rev. Lett.* **55** 2160 (1985)
14. Franz G, Freyland W, Hensel F *J. Phys. Colloques* **41** (C8) C8-70 (1980)
15. Pfeifer H P, Freyland W, Hensel F *Ber. Bunsenges. Phys. Chem.* **83** 204 (1979)
16. Kikoin I K, Senchenkov A P *Fiz. Met. Metalloved.* **24** 843 (1967)
17. Götzlaff W, Schönherr G, Hensel F *Z. Phys. Chem.* **156** 219 (1988)
18. Ohse R W (Ed.) *Handbook of Thermodynamic and Transport Properties of Alkali Metals* (New York: Wiley, 1985)
19. Hensel F, Marceca E, Pilgrim W C *J. Phys. Condens. Matter* **10** 11395 (1998)
20. Alekseev V A, Vedenov A A *Sov. Phys. Usp.* **13** 830 (1970); *Usp. Fiz. Nauk* **102** 665 (1970)
21. Likal'ter A A *Teplofiz. Vys. Temp.* **16** 1219 (1978)
22. Khrapak A G *Teplofiz. Vys. Temp.* **17** 1147 (1979)
23. Yakubov I T *Dokl. Akad. Nauk SSSR* **247** 841 (1979)
24. Zhukhovitskii D I *Zh. Fiz. Khim.* **67** 1962 (1993)
25. Ali (Basu) M et al. *J. Chem. Phys.* **124** 024325 (2006)
26. Khomkin A L, Shumikhin A S *High Temp.* **51** 594 (2013); *Teplofiz. Vys. Temp.* **51** 663 (2013)
27. Semenov A M, Petkoglo N P, Zakharova O D *High Temp.* **46** 337 (2008); *Teplofiz. Vys. Temp.* **46** 374 (2008)
28. Likal'ter A A *Sov. Phys. Usp.* **35** 591 (1992); *Usp. Fiz. Nauk* **162** (7) 119 (1992)
29. Likal'ter A A *Phys. Usp.* **43** 777 (2000); *Usp. Fiz. Nauk* **170** 831 (2000)
30. Likalter A A, Schneidenbach H *Physica A* **277** 293 (2000)
31. Lang G *Z. Metallkd.* **68** 213 (1977)
32. Apfelbaum E M, Vorob'ev V S *J. Chem. Phys.* **139** 046101 (2013)
33. Apfelbaum E M, Vorob'ev V S *J. Phys. Chem. B* **119** 11825 (2015)
34. Apfelbaum E M, Vorob'ev V S *J. Phys. Chem. B* **120** 4828 (2016)
35. Fortov V E, Dremin A N, Leont'ev A A *Teplofiz. Vys. Temp.* **13** 1072 (1975)
36. Young D A, Alder B J *Phys. Rev. A* **3** 364 (1971)
37. Likal'ter A A *Teplofiz. Vys. Temp.* **23** 465 (1985)
38. Bushman A V, Fortov V E *Sov. Phys. Usp.* **26** 465 (1983); *Usp. Fiz. Nauk* **140** 177 (1983)
39. Fortov V E et al. *Nucl. Instrum. Meth. Phys. Res. A* **415** 604 (1998)
40. Bardeen J *J. Chem. Phys.* **6** 367 (1938)
41. Kuhn T S *Phys. Rev.* **79** 515 (1950)
42. Kuhn T S, Van Fleck J H *Phys. Rev.* **79** 382 (1950)
43. Wigner E, Hangtington H *J. Chem. Phys.* **3** 764 (1935)
44. Kratzer A *Z. Phys.* **3** 289 (1920)
45. Daw M S, Baskes M I *Phys. Rev. B* **29** 6443 (1984)
46. Slater J C, Koster G F *Phys. Rev.* **94** 1498 (1954)
47. Banerjia A, Smith J R *Phys. Rev. B* **37** 6632 (1988)
48. Rose J H et al. *Phys. Rev. B* **29** 2963 (1984)
49. DeSilva A W, Kunze H-J *Phys. Rev. E* **49** 4448 (1994)
50. DeSilva A W, Katsouros J D *Phys. Rev. E* **57** 5945 (1998)
51. Krisch I, Kunze H-J *Phys. Rev. E* **58** 6557 (1998)
52. DeSilva A W, Katsouros J D *J. Physique IV* **10** 209 (2000)
53. Clérouin J et al. *Phys. Rev. B* **78** 224203 (2008)
54. Clérouin J et al. *Phys. Plasmas* **19** 082702 (2012)
55. Korobenko V N, Rakhel A D *J. Exp. Theor. Phys.* **112** 649 (2011); *Zh. Eksp. Teor. Fiz.* **139** 746 (2011)
56. Korobenko V N, Rakhel A D *Phys. Rev. B* **88** 134203 (2013)
57. Kondrat'ev A M, Korobenko V N, Rakhel A D *J. Exp. Theor. Phys.* **127** 1074 (2018); *Zh. Eksp. Teor. Fiz.* **154** 1168 (2018)
58. Ternovoi V Ya, Fortov V E, Kvitov S V, Nikolaev D N *AIP Conf. Proc.* **370** 81 (1996)
59. Emelyanov A N, Nikolaev D N, Ternovoi V Ya *High Temp. High Press.* **37** 279 (2008)
60. Desjarlais M P, Kress J D, Collins L A *Phys. Rev. E* **66** 025401 (2002)
61. Mazevet S et al. *Phys. Rev. E* **71** 016409 (2005)
62. French M, Mattsson T R *Phys. Rev. B* **90** 165113 (2014)
63. Miljacic L et al. *Calphad* **51** 133 (2015)
64. Knyazev D V, Levashov P R *Phys. Plasmas* **21** 073302 (2014)
65. Minakov D V, Paramonov M A, Levashov P R *Phys. Rev. B* **97** 024205 (2018)
66. Minakov D V, Paramonov M A, Levashov P R *AIP Adv.* **8** 125012 (2018)
67. Li D et al. *Sci. Rep.* **4** 5898 (2014)
68. Ding Y H, Hu S X *Phys. Plasmas* **24** 062702 (2017)
69. Migdal K P et al. *Appl. Surf. Sci.* **478** 818 (2019)
70. Zhang S et al. *J. Chem. Phys.* **146** 074505 (2017)
71. Driver K P et al. *High Energy Density Phys.* **23** 81 (2017)
72. Ovechkin A A, Loboda P A, Falkov A L *High Energy Density Phys.* **20** 38 (2016)
73. Hou Y et al. *High Energy Density Phys.* **22** 21 (2017)
74. Redmer R *Phys. Rev. E* **59** 1073 (1999)
75. Kuhlbrodt S, Holst B, Redmer R *Contrib. Plasma Phys.* **45** 73 (2005)
76. Apfelbaum E M *Czech. J. Phys.* **56** B618 (2006)
77. Apfelbaum E M *Contrib. Plasma Phys.* **56** 176 (2016)
78. Apfelbaum E M *Contrib. Plasma Phys.* **57** 479 (2017)
79. Fu Z J et al. *Phys. Scr.* **85** 045502 (2012)
80. Norman G E, Starostin A N *High Temp.* **8** 381 (1970); *Teplofiz. Vys. Temp.* **8** 413 (1970)
81. Ebeling W, Norman G E *J. Stat. Phys.* **110** 861 (2003)
82. Filinov V S et al. *Contrib. Plasma Phys.* **44** 388 (2004)
83. Filinov V S et al. *Contrib. Plasma Phys.* **43** 290 (2003)
84. Mintsev V B, Fortov V E *JETP Lett.* **30** 375 (1979); *Pis'ma Zh. Eksp. Teor. Fiz.* **30** 401 (1979)
85. Gatilov L A et al. *J. Appl. Mech. Tech. Phys.* **26** 88 (1985); *Prikl. Mekh. Tekh. Fiz.* (1) 99 (1985)
86. Urlin V D, Mochalov M A, Mikhailova O L *High Press. Res.* **8** 595 (1992)
87. Glukhodedov V D et al. *J. Exp. Theor. Phys.* **89** 292 (1999); *Zh. Eksp. Teor. Fiz.* **116** 551 (1999)
88. Fortov V E et al. *Sov. Phys. JETP* **44** 116 (1976); *Zh. Eksp. Teor. Fiz.* **71** 225 (1976)
89. Mintsev V B, Fortov V E, Gryaznov V K *Sov. Phys. JETP* **52** 59 (1980); *Zh. Eksp. Teor. Fiz.* **79** 116 (1980)
90. Preising M et al. *Phys. Plasmas* **25** 012706 (2018)
91. Li Z-G et al. *Phys. Plasmas* **23** 052701 (2016)
92. Sun H et al. *J. Chem. Phys.* **144** 124503 (2016)
93. Wang Z-Q et al. *Phys. Rev. E* **100** 033214 (2019)
94. Adams J R et al. *Phys. Rev. E* **76** 036405 (2007)
95. Rosmej S, Reinholz H, Röpke G *Phys. Rev. E* **95** 063208 (2017)
96. Fu Z J, Chen Q F, Chen X R *Contrib. Plasma Phys.* **52** 251 (2012)
97. Apfelbaum E M *Contrib. Plasma Phys.* **51** 395 (2011)
98. Da Silva L B et al. *Phys. Rev. Lett.* **78** 483 (1997)
99. Knudson M D et al. *Phys. Rev. Lett.* **87** 225501 (2001)
100. Holmes N C, Ross M, Nellis W J *Phys. Rev. B* **52** 15835 (1995)
101. Belov S I et al. *JETP Lett.* **76** 433 (2002); *Pis'ma Zh. Eksp. Teor. Fiz.* **76** 508 (2002)
102. Weir S T, Mitchell A C, Nellis W J *Phys. Rev. Lett.* **76** 1860 (2002)
103. Fortov V E, Khrapak A G, Yakubov I T *Fizika Neideal'noi Plazmy* (Nonideal Plasma Physics) (Moscow: Fizmatlit, 2010)
104. Fortov V E et al. *Phys. Rev. Lett.* **99** 185001 (2007)
105. Redmer R et al. *J. Phys. Condens. Matter* **4** 1659 (1992)
106. Apfelbaum E M *Phys. Chem. Liq.* **48** 534 (2010)
107. Clementi E, Roetti C *Atom. Data Nucl. Data Tabl.* **14** 177 (1974)
108. Khomkin A L, Shumikhin A S *J. Exp. Theor. Fiz.* **123** 891 (2016); *Zh. Eksp. Teor. Fiz.* **150** 1020 (2016)
109. Puska M J, Nieminen R M *Phys. Rev. B* **43** 12221 (1991)
110. Yxklinten U, Hartford J, Holmquist T *Phys. Scr.* **55** 499 (1997)
111. Belashchenko D K *Phys. Usp.* **56** 1176 (2013); *Usp. Fiz. Nauk* **183** 1281 (2013)
112. Regel A R, Ioffe A F *Prog. Semicond.* **4** 237 (1960)
113. Khomkin A L, Shumikhin A S *J. Exp. Theor. Fiz.* **124** 70 (2017); *Zh. Eksp. Teor. Fiz.* **151** 82 (2017)
114. Khomkin A L, Shumikhin A S *J. Exp. Theor. Fiz.* **118** 72 (2014); *Zh. Eksp. Teor. Fiz.* **145** 84 (2014)

115. Stishov S M *Phys. Rev. B* **47** 12260 (1993)
116. Khomkin A L, Shumikhin A S *J. Exp. Theor. Fiz.* **121** 521 (2015); *Zh. Eksp. Teor. Fiz.* **148** 597 (2015)
117. Khomkin A L, Shumikhin A S *Contrib. Plasma Phys.* **56** 228 (2016)
118. Khomkin A L, Shumikhin A S *High Temp. High Press.* **46** 367 (2017)
119. Khomkin A L, Shumikhin A S *High Temp. High Press.* **49** 143 (2020)
120. Gathers G R *Rep. Prog. Phys.* **49** 341 (1986)
121. Seydel U, Fischer U *J. Phys. F* **8** 1397 (1978)
122. Martynyuk M M *Zh. Fiz. Khim.* **57** 810 (1983)
123. Hixson R S, Winkler M A *Int. J. Thermophys.* **13** 477 (1992)
124. Pottlacher G, Kaschnitz E, Jager H *J. Phys. Condens. Matter* **3** 5783 (1991)
125. Keldysh L V *Sov. Phys. Usp.* **13** 292 (1970); *Usp. Fiz. Nauk* **100** 514 (1970)
126. Thomas G A, Rice T M, Hencel J C *Phys. Rev. Lett.* **33** 219 (1974)
127. Ross M *Phys. Rev. B* **58** 669 (1998)
128. Iosilevskiy I L *J. Phys. Conf. Ser.* **653** 012077 (2015)
129. Gryaznov V K, Iosilevskiy I L *J. Phys. A* **42** 214007 (2009)
130. Mulenko I A, Khomkin A L, Shumikhin A S *High Temp.* **42** 842 (2004); *Teplofiz. Vys. Temp.* **42** 835 (2004)
131. Khomkin A L, Shumikhin A S *Vestn. OIVT* **2** (1) 19 (2019)
132. Filippov A V, Starostin A N, Gryaznov V K *J. Exp. Theor. Phys.* **126** 430 (2018); *Zh. Eksp. Teor. Fiz.* **153** 514 (2018)
133. Khomkin A L, Shumikhin A S *J. Exp. Theor. Fiz.* **124** 1001 (2017); *Zh. Eksp. Teor. Fiz.* **151** 1169 (2017)
134. Khomkin A L *Teplofiz. Vys. Temp.* **16** 37 (1978)
135. Khomkin A L, Shumikhin A S *High Temp.* **50** 307 (2012); *Teplofiz. Vys. Temp.* **50** 329 (2012)
136. Radzig A A, Smirnov B M *Reference Data on Atoms, Molecules, and Ions* (Springer Series in Chemical Physics, Vol. 31) (Berlin: Springer-Verlag, 1985); Translated from Russian: *Spravochnik po Atomnoi i Molekulyarnoi Fizike* (Moscow: Atomizdat, 1980)
137. Khomkin A L, Shumikhin A S *Plasma Phys. Rep.* **44** 958 (2018); *Fiz. Plazmy* **44** 832 (2018)
138. Hirschfelder J O, Curtiss C F, Bird R B (Eds) *Molecular Theory of Gases and Liquids* (New York: Wiley, 1954)
139. Khomkin A L, Shumikhin A S *J. Exp. Theor. Phys.* **130** 602 (2020); *Zh. Eksp. Teor. Fiz.* **157** 717 (2020)
140. Kloss A et al. *Phys. Rev. E* **54** 5851 (1996)
141. Onufriev S V *High Temp.* **49** 205 (2011); *Teplofiz. Vys. Temp.* **49** 213 (2011)
142. Leitner M, Schröer W, Pottlacher G *Int. J. Thermophys.* **39** 124 (2018)
143. Boboridis K, Pottlacher G, Jäger H *Int. J. Thermophys.* **20** 1289 (1999)